

# Supplementary Information

## **Concurrent electrode-electrolyte interfaces engineering via nano-Si<sub>3</sub>N<sub>4</sub> additive for high-rate, high-voltage lithium metal batteries**

Jinuk Kim<sup>a,‡</sup>, Dong Gyu Lee<sup>b,‡</sup>, Ju Hyun Lee<sup>a,‡</sup>, Saehun Kim<sup>a,‡</sup>, Cheol-Young Park<sup>a</sup>, Jiyeon Lee<sup>b</sup>, Hyeokjin Kwon<sup>a</sup>, Hannah Cho<sup>a</sup>, Jungyoon Lee<sup>a</sup>, Donghyeok Son<sup>a</sup>, Hee-Tak Kim<sup>a</sup>, Nam-Soon Choi<sup>a,\*</sup>, Tae Kyung Lee<sup>b,\*</sup>, and Jinwoo Lee<sup>a,\*</sup>

<sup>a</sup>Department of Chemical and Biomolecular Engineering, Korea Advanced Institute of Science and Technology (KAIST), 291 Daehak-ro, Daejeon 34141, Republic of Korea.

<sup>b</sup>Department of Materials Engineering and Convergence Technology, Gyeongsang National University (GNU), 501 Jinju-daero, Jinju 52828, Republic of Korea.

\*e-mail: nschoi@kaist.ac.kr (Nam-Soon Choi), tklee8865@gnu.ac.kr (Tae Kyung Lee), jwlee1@kaist.ac.kr (Jinwoo Lee)

# **Contents**

- 1. Supplementary Methods**
- 2. Supplementary Figures**
- 3. Supplementary Tables**
- 4. Supplementary Note**
- 5. Supplementary References**

## 1. Supplementary Methods

**Electrolyte preparation.** Electrolytes were prepared in an argon-filled glovebox ( $O_2 < 0.1\text{ppm}$ ,  $H_2O < 0.1\text{ppm}$ ). 1M  $LiPF_6$  EC/DEC + 10 wt% (Blank) was purchased from Dongwha Electrolyte. Nano- $Si_3N_4$  (nanopowder, Average particle size, APS < 50nm, purity > 98.5%) and nano- $SiO_2$  (nanopowder, particle size: 40~60 nm, purity > 99.9%) was purchased from Sigma-aldrich and Dittotechnology, respectively. Other nitrides including BN (hexagonal, APS: 70nm, purity > 99.85%), TiN (APS: 20 nm, purity > 99.2%), VN (APS: 40 nm, Purity > 99.9%) were purchased from Nanografi.  $Li_3N$  (APS: 80 – 100 nm, purity: 99%) was purchased from Nanoshel. CoO (APS: 50 nm, purity > 99.5%) and  $TiO_2$  (anatase, particle size < 25 nm, purity > 99.7%) were purchased from Sigma-aldrich. Nanopowders were dried under vacuum, at 110 °C overnight. After drying, the Blank was added to meet the prescribed additive concentration and stirred vigorously overnight.

**Electrochemical tests.** Electrochemical tests were conducted using CR-2032 type coin-cell (Wellcos), except pouch-cell tests. For coin cell fabrications, 20  $\mu\text{L}$  of electrolyte and a Celgard 2400 polypropylene separator were employed, including Li||Cu half-cell, Li||Li symmetric cell. Li metal with thicknesses of 200  $\mu\text{m}$ , 50  $\mu\text{m}$ , and 40  $\mu\text{m}$  was purchased from Honjo Metal, and unless stated otherwise, 200  $\mu\text{m}$  Li was used. For the modified Aurbach's C.E. tests<sup>34</sup>, Li metal was initially plated at 6 mAh  $\text{cm}^{-2}$  on a 14  $\Phi$  Cu current collector. After complete stripping, a second plating was performed for 6 mAh  $\text{cm}^{-2}$ . Subsequently, 9 cycles were executed under conditions of 2 mA  $\text{cm}^{-2}$  and 1 mA h  $\text{cm}^{-2}$ . Finally, the electrochemically active Li was completely stripped via a cut-off voltage of 1 V. All procedures were conducted at a current density of 2 mA  $\text{cm}^{-2}$ . Tafel plots were obtained by Li||Li symmetric cells, with 0.5  $\text{mV s}^{-1}$  of scan rate and -0.15-0.15V of voltage range. For Li||NCM811 full-cells, NCM811 sheets (active material/Super P C65/Polyvinylidene fluoride = 96:2:2, active material mass loading: 18.78  $\text{mg cm}^{-2}$ , 3.8 mAh  $\text{cm}^{-2}$ ) were provided by LG Energy Solution. Unless noted otherwise, 23.4  $\mu\text{L}$  (E/C = 4  $\mu\text{L mAh}^{-1}$ ) of electrolyte was injected for the coin-type full cell. For pouch cell fabrications, two Li metal anodes (40  $\mu\text{m}$ ), two Cu foils, and double-side-coated NMC811 (3.8 mAh  $\text{cm}^{-2}$  for single side) were cut into 40 mm  $\times$  60 mm and 30 mm  $\times$  50 mm, respectively. Ni and Al tabs were welded onto the Cu foil and NCM811, respectively, using a welding machine (WC-TW-300SJ, Wellcos). Electrodes and separators were stacked, sealed into pouches, and injected with 2.5 g  $\text{Ah}^{-1}$  of electrolyte in the Ar-filled glovebox. Galvanostatic tests, including both coin and pouch cells, were conducted using a battery cycler (WonATech). EIS tests were performed at potentiostat (Biologics). An applied sine wave with an amplitude of 10 mV ranged from 10 mHz to 100 kHz. The chemical corrosion of each electrolyte was tested using the same procedure as in the literature<sup>1</sup>. Electrochemical tests were conducted at 30°C.

**Electrolyte characterizations.**  $^7\text{Li}$  and  $^{19}\text{F}$  NMR measurements were performed using a 600 MHz liquid NMR spectrometer (Avance Neo 600, Prodigy probe).  $^7\text{Li}$  NMR were conducted using NMR coaxial inserts, with the inner tube containing a 1M LiCl  $D_2O$  reference solution.  $^{19}\text{F}$  NMR were conducted using the reference solution containing 1 wt%  $C_6F_6$  in  $d_8$ -THF. Raman spectra was obtained by LabRAM HR Evolution Visible\_NIR (HORIBA) with 514 nm excitation laser. The solvents were sealed in quartz vials. H-cell tests to measure the relative Gibbs solvation energy were conducted following the procedure outlined in the literature<sup>2</sup>.

**Post-mortem analysis.** Post-mortem analyses were conducted after the galvanostatic cycling. After cycling, the coin-cells were disassembled, and the electrodes were carefully rinsed with DEC. The electrodes were then thoroughly dried in the antechamber of the glovebox. SEM images were acquired using Magellan400 (FEI company) with an acceleration voltage of 10 kV and an electron beam current of 0.20 nA. Air exposure was minimized during sample transfer (under 5s). FIB-SEM cross-sectional images were acquired using Helios Nanolab 450 F1 (FEI company). Cross-sectional cleaning was conducted at 5 kV and 0.3 mA to eliminate the damaged layer caused by Ga ions. XPS results were obtained using K-alpha (Thermo VG Scientific) with an X-ray source (Al,  $h\nu = 1,486.7$  eV). Samples were transferred by using vacuum transfer holder (Thermo Fisher Scientific) to avoid air exposure. Depth profiling was conducted using an Ar<sup>+</sup> ion beam for sample sputtering. Cryo-TEM analysis was conducted using a Glacios (Thermo Fisher) with a 200 kV accelerating voltage. The samples were transferred to the cryo-autoloader (Glacios) in liquid nitrogen to avoid air exposure. 0.17 mA h cm<sup>-2</sup> of Li was deposited on the uncoated Cu grid (200 mesh). The acquired images and FFT patterns were analyzed using Gatan DigitalMicrograph software. The d-spacing information of crystalline materials were provided by Materials Project<sup>3</sup>. HADDF-STEM images of cycled NCM811 were acquired using the Titan 80-300 S/TEM microscope (FEI) at 300 kV, while HRTEM images for CEI layer analysis were obtained using TEM-ARM200F (JEOL) with a 200 kV accelerating voltage. TEM specimens were prepared using Helios Nanolab 450 F1 (FEI company) with a standard lift-out procedure. For NCM811 and CEI layer observations, C and Pt layer was deposited to avoid Ga ion-beam damage in the subsequent lift-out and thinning process, respectively. TOF-SIMS analysis was performed using TOF.SIMS-5 (Ion-TOF) following the sampling procedures. To minimize air exposure during sample transfer, an Ar-filled plastic bag was used. TOF-SIMS measurements were conducted in negative mode, with Cs<sup>+</sup> (3 keV, 20 nA) as the sputtering source to generate secondary ions. For depth profiling, a Bi<sup>3+</sup> ion beam (30 keV, 0.6 pA) was employed. The sputtering and analysis areas were set at 200  $\mu\text{m} \times 200 \mu\text{m}$  and 50  $\mu\text{m} \times 50 \mu\text{m}$ , respectively. 3D reconstruction images were obtained after 500 seconds of sputtering, and the z-axis depth is a theoretical value calculated under the same sputtering conditions applied to lithium metal. XRD patterns were obtained using SmartLab (Rigaku, Cu K $\alpha$ ) with a scanning rate of 4.00° min<sup>-1</sup>.

**Molecular dynamics (MD) simulations.** MD simulations were performed to investigate the solvation characteristics of the Blank and 3-SN electrolyte systems. An electrostatic potential charge<sup>4</sup> was adopted as the atomic charges of all electrolyte molecules obtained from density functional theory (DFT) calculations. Based on previous studies<sup>5,6</sup>, the atomic charges of Li<sup>+</sup> cation and PF<sub>6</sub><sup>-</sup> anion were scaled by using the refractive indices of EC (1.420) and DEC (1.384). The scaling factor of atomic charges was 0.713 for our electrolyte systems (*i.e.*, EC/DEC 1:1 vol%). The method of atom-based summation with a cut-off distance of 12.5 Å was used for van der Waals interactions, and the particle–particle particle–mesh method with a 0.001 kcal mol<sup>-1</sup> accuracy was used for electrostatic interactions. All MD simulations were performed using COMPASS III forcefield<sup>7</sup> at 298.15 K and 1 atm conditions. The *NPT* ensemble (isothermal-isobaric ensemble) was simulated for 5 ns with a 1.0 fs time step using Berendsen of thermostat and barostat<sup>8</sup>. The *NVT* ensemble (canonical ensemble) was simulated for 800 ns with a 1 fs time step using Berendsen of thermostat<sup>8</sup>.

**Density functional theory (DFT) calculations.** For the calculation of the atomic charges of the electrolyte (*i.e.*, EC, DEC, FEC, LiPF<sub>6</sub>, and nano-Si<sub>3</sub>N<sub>4</sub> clusters), DMol<sup>3</sup> program<sup>9,10</sup> was utilized. The Becke's three-parameter

hybrid exchange functional with Lee–Yang–Parr correlation functional<sup>11, 12</sup> was used for the exchange-correlation energy with the spin polarization. The Tkatchenko and Scheffler (TS) method<sup>13</sup> was adopted for the van der Waals interactions. All electron relativistic core treatment and double numerical plus polarization basis set (version 4.4) were used to describe the core electrons and atomic orbital basis set, respectively. For the geometry optimization, the convergence criteria of energy, force, displacement, and self-consistent field were set to  $1 \times 10^{-5}$  Ha, 0.002 Ha/Å, 0.005 Å, and  $1 \times 10^{-6}$  Ha, respectively. An implicit environment was applied by using the conductor-like screening model<sup>14</sup> method with the dielectric constant of 20.89 (*i.e.*, EC/DEC, 1:1 vol%, dielectric constants = 95.3 (EC) and 2.82 (DEC) at 25 °C<sup>15</sup>), which was calculated using the mixing rule<sup>16</sup>.

For the calculation of the binding energies of electrolyte molecules on  $\alpha$ -phase Si<sub>3</sub>N<sub>4</sub> (101) surface using the CASTEP program<sup>17</sup>. The generalized gradient approximation with Perdew-Burke-Ernzerhof functional<sup>18</sup> was employed for the exchange-correlation energy. For the cell and geometry optimizations, the ultrasoft and TS methods were utilized for pseudopotential and van der Waals correction, respectively, with the spin polarization. Broyden–Fletcher–Goldfarb–Shanno method was used as for the cell and geometry optimizations. For the cell and geometry optimizations, the convergence criteria of energy, force, stress, displacement and self-consistent field were set to  $1 \times 10^{-5}$  eV/atom, 0.03 eV/Å, 0.05 GPa,  $1 \times 10^{-3}$  Å, and  $1 \times 10^{-6}$  eV/atom, respectively. The value of energy cut-off was set to 340 eV. Moreover,  $5 \times 5 \times 6$  *k*-points and gamma point were used with the Monkhorst-Pack grid<sup>19</sup> for the cell optimization of  $\alpha$ -phase Si<sub>3</sub>N<sub>4</sub> unit cell and the geometry optimization of Si<sub>3</sub>N<sub>4</sub> (101) surface systems, respectively.

The binding energy was calculated by following equation;  $E_{\text{binding}} = E_{\text{total}} - E_{\text{surface}} - E_{\text{electrolyte}}$

where  $E_{\text{total}}$ ,  $E_{\text{surface}}$ , and  $E_{\text{electrolyte}}$  are the energy of bound system on the Si<sub>3</sub>N<sub>4</sub> surface, the energy of Si<sub>3</sub>N<sub>4</sub> surface system, and the energy of electrolyte molecule, respectively.

The bond dissociation energy (BDE) was calculated by following equation;  $E_{\text{BDE}} = E_{\text{H-dissociated}} + E_{\text{hydrogen}} - E_{\text{pristine}}$

where  $E_{\text{H-dissociated}}$  is the energy of hydrogen dissociated system,  $E_{\text{hydrogen}}$  is the energy of the hydrogen atom, and  $E_{\text{pristine}}$  is the energy of pristine system, respectively.

## 2. Supplementary Figures

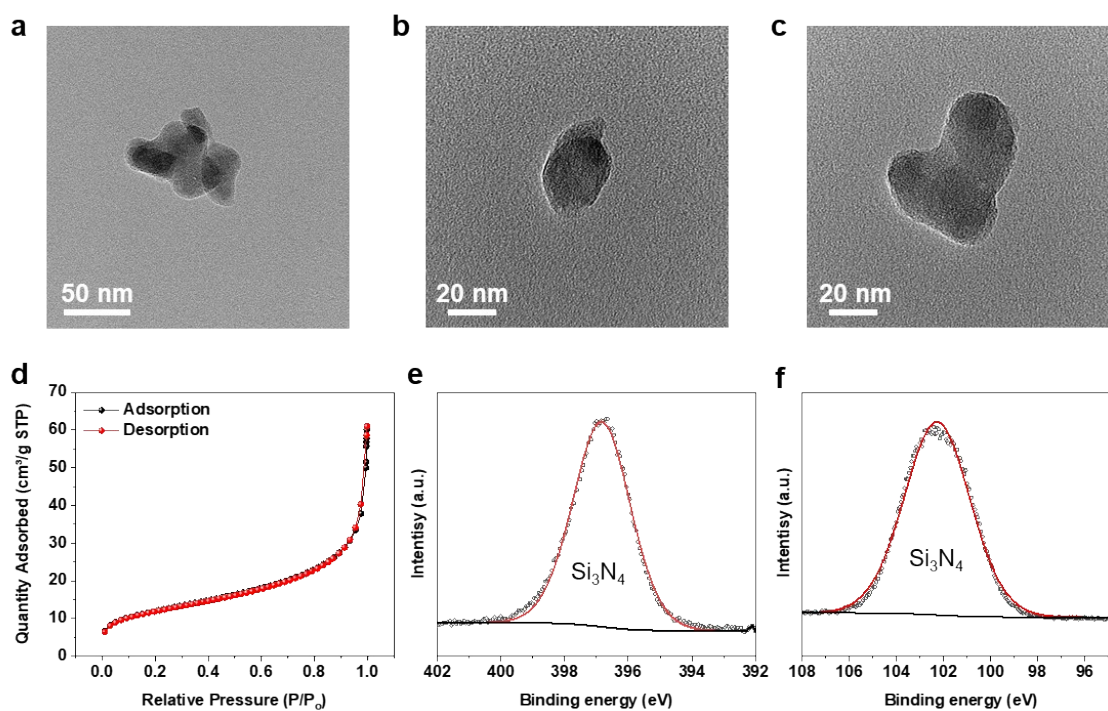


**Fig. S1.** Basic properties of nano-Si<sub>3</sub>N<sub>4</sub>. **(a)-(c)** TEM images of nano-Si<sub>3</sub>N<sub>4</sub>. The particle size of nano-Si<sub>3</sub>N<sub>4</sub> is below 50 nm. **(d)** Adsorption-desorption isotherm linear plot of nano-Si<sub>3</sub>N<sub>4</sub>. The adsorption-desorption isotherm displays a type III hysteresis loop, indicating that the nano-Si<sub>3</sub>N<sub>4</sub> is non-porous. **(e)** N 1s XPS spectrum of nano-Si<sub>3</sub>N<sub>4</sub>. **(f)** Si 2p XPS spectrum of nano-Si<sub>3</sub>N<sub>4</sub>.

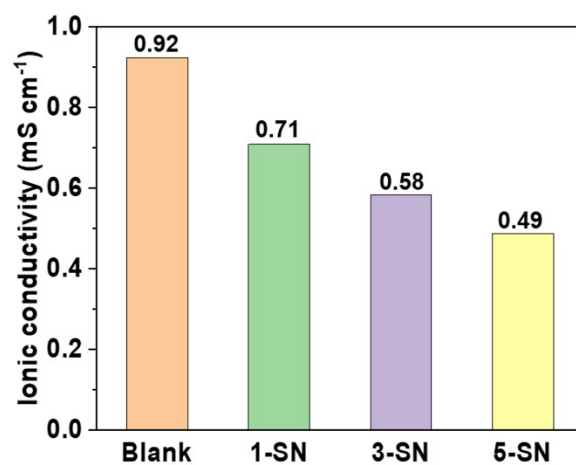


**Fig. S2.** Measured ionic conductivities of various nano-Si<sub>3</sub>N<sub>4</sub> concentrations in the Blank (x-SNs) using SSISS symmetric cell with separator through electrochemical impedance spectroscopy (EIS) tests.

**Note)** With increasing concentration of nano-Si<sub>3</sub>N<sub>4</sub>, a slight decrease was observed in ionic conductivity owing to weak Li<sup>+</sup> solvation caused by nano-Si<sub>3</sub>N<sub>4</sub>. This may adversely affect the rate capability, wettability, and viscosity of the electrolyte, necessitating the determination of the optimal concentration.

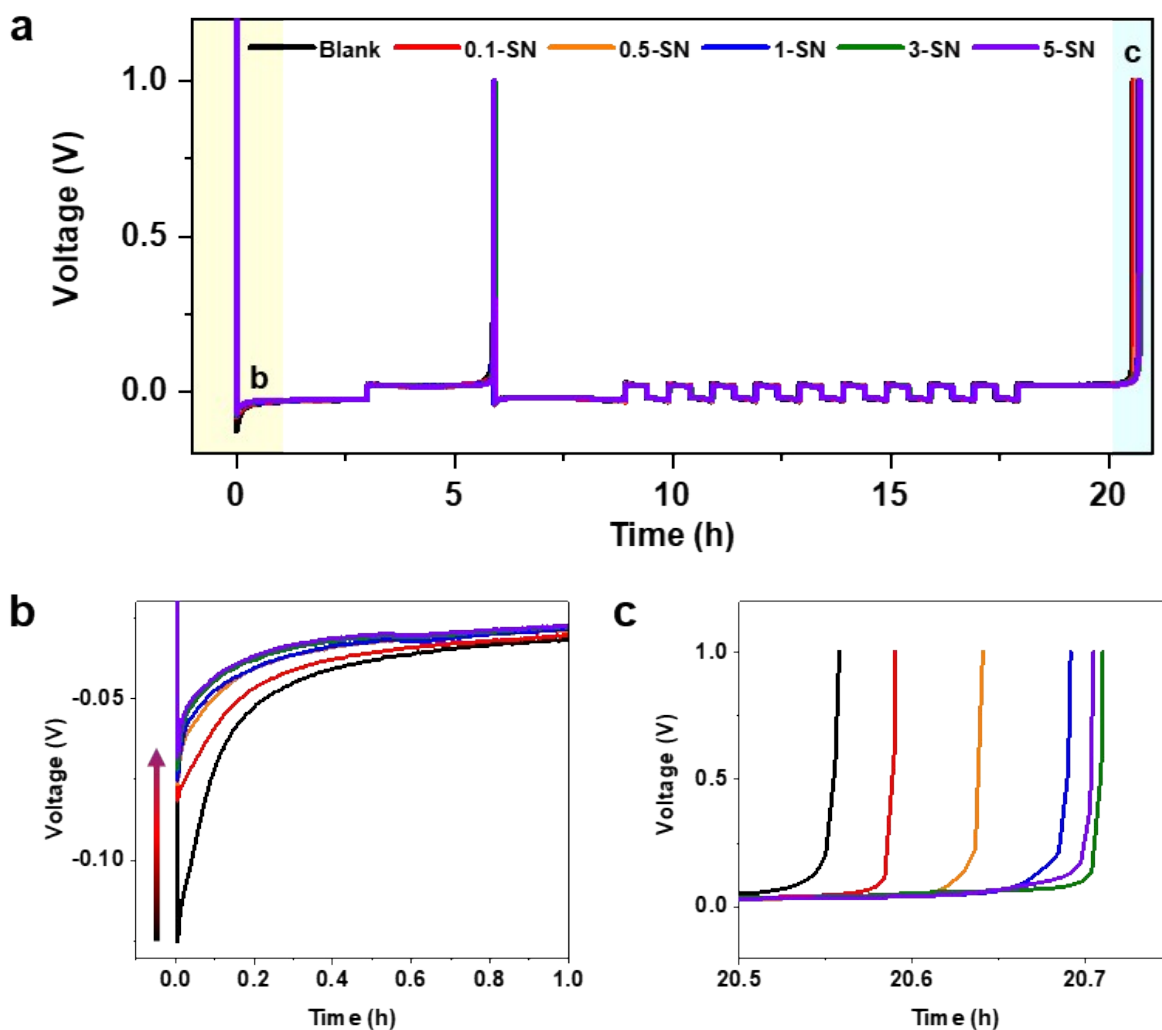


**Fig. S3.** (a) Modified Aurbach's Coulombic efficiency tests of various x-SNs at  $2 \text{ mA cm}^{-2}$ . (b) Enlargements of (a) for displaying nucleation overpotential. (c) Enlargements of (a) for displaying Coulombic efficiency.

**Note)** An excessive amount of nano- $\text{Si}_3\text{N}_4$  can lead to reduced ionic conductivity (Fig. S2), increased viscosity, and decreased wettability of the electrodes and separator. Furthermore, with increasing in nano- $\text{Si}_3\text{N}_4$  concentration, the impact on  $\text{Li}^+$  solvation progressively diminished. Therefore, based on a comprehensive evaluation of the electrolyte properties (Fig. 2a, Fig. 2b, Fig. S2) and modified Aurbach's Coulombic efficiency tests (Fig. S3), 3-SN was considered to be the optimal concentration.

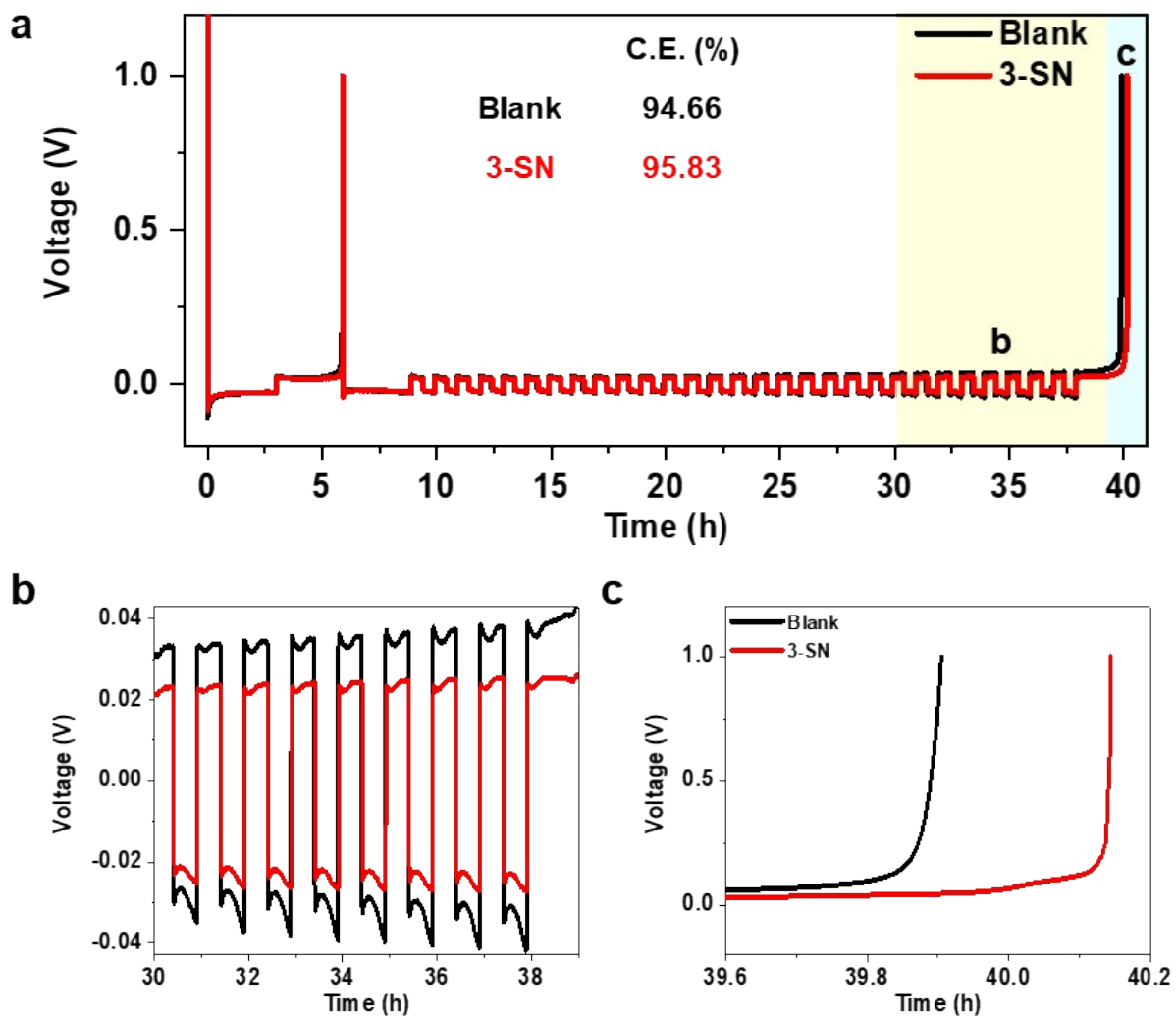


**Fig. S4.** (a) Modified Aurbach's Coulombic efficiency tests of the Blank and 3-SN at 2 mA cm<sup>-2</sup> for 29 cycles. (b) Enlargements of (c) for displaying nucleation overpotential. (c) Enlargements of (a) for displaying Coulombic efficiency.

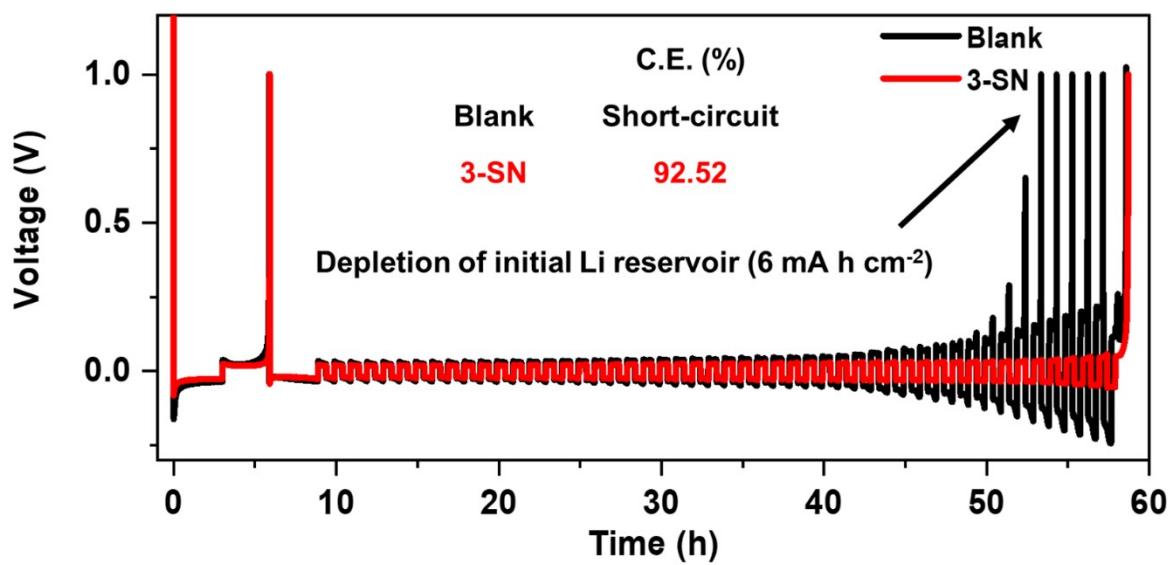
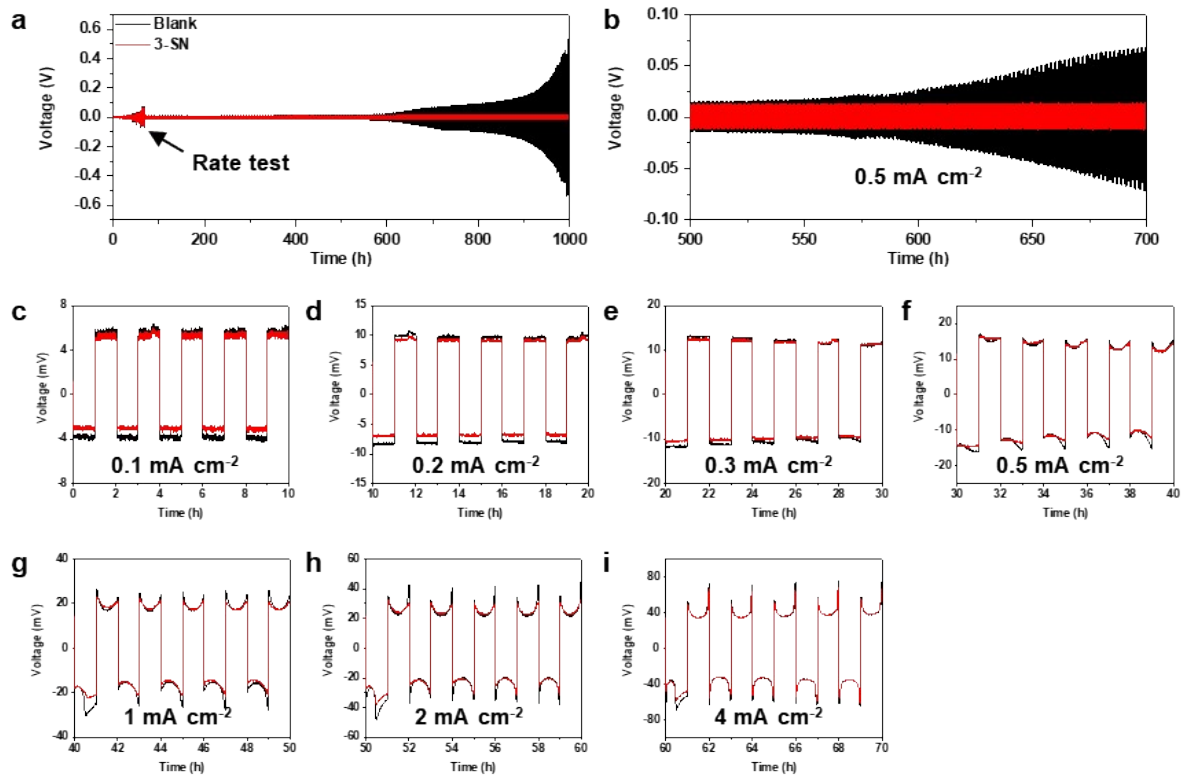


Fig. S5. Modified Aurbach's Coulombic efficiency tests of the Blank and 3-SN at 2 mA cm<sup>-2</sup> for 49 cycles.



**Fig. S6.** (a) Rate tests under various current densities in L1Li symmetric cells. (b) Enlargements of (a) for visualizing the long-term stability of 3-SN. (c)-(i), Enlargements of (a) for visualizing each current densities.

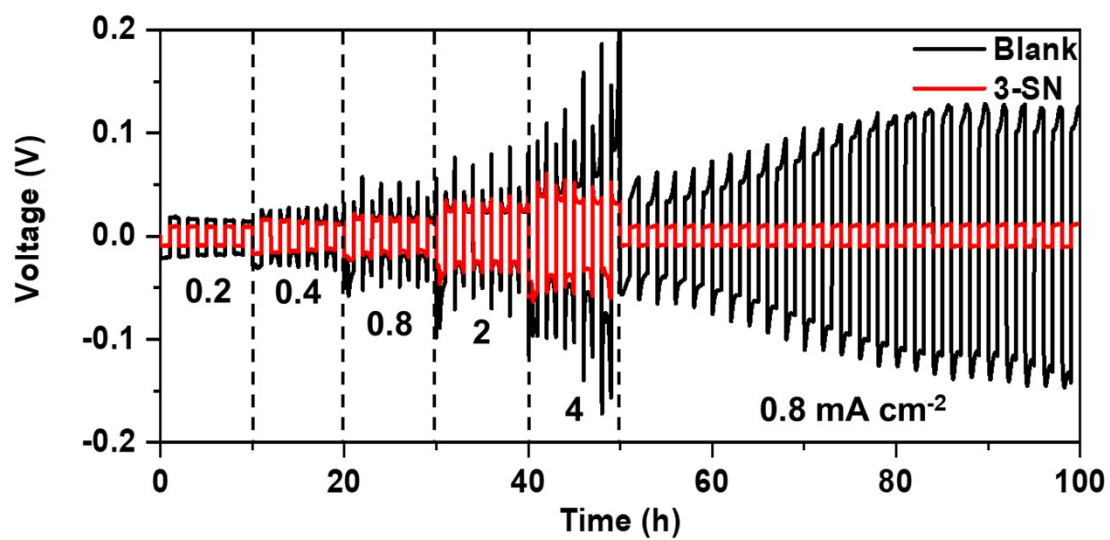


Fig. S7. Rate tests under various current densities in LiLi symmetric cells.

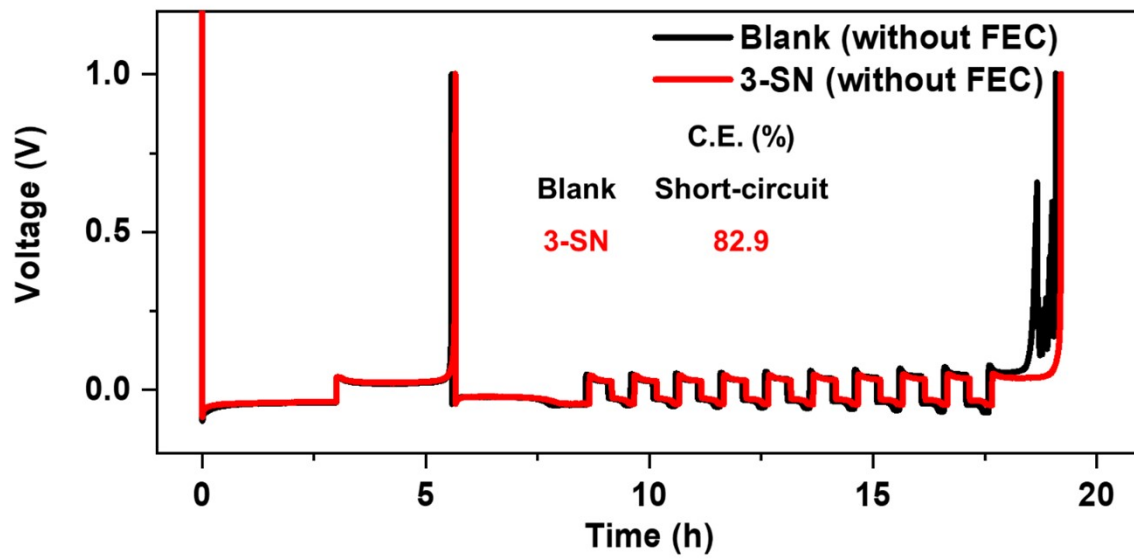
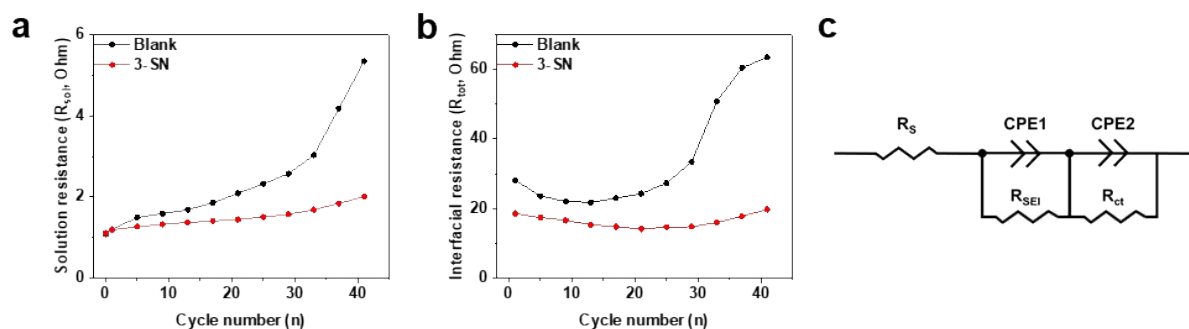
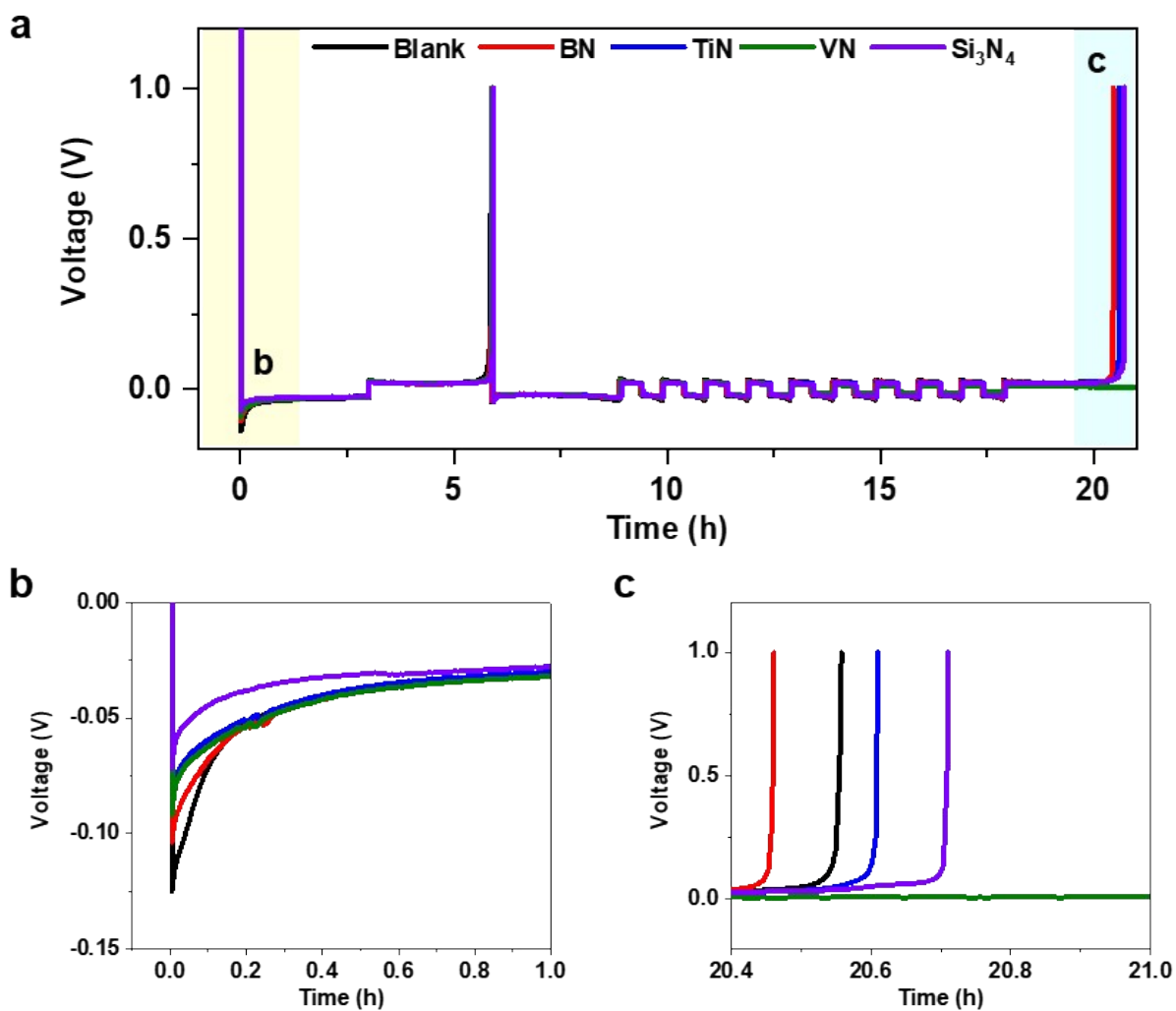


Fig. S8. Modified Aurbach's Coulombic efficiency tests without FEC at  $2 \text{ mA cm}^{-2}$ .



**Fig. S9.** EIS tests of Li|Li symmetric cells during cycling under  $2 \text{ mA cm}^{-2}$  and  $1 \text{ mA h cm}^{-2}$ . **(a)** Measured solution resistance for each cycle number. **(b)** Measured interfacial resistance for each cycle number. **(c)** Equivalent circuit model for EIS tests.

**Note)** Before cycling, the solution resistance of the Blank was slightly lower than that of 3-SN (**Table S3-S4**), primarily because of marginally higher ionic conductivity of the Blank, as indicated in **Fig. S2**. However, as the number of cycles increased, the solution resistance of the Blank increased rapidly, whereas that of 3-SN experiences a slight increase (**Fig. S9a**). This phenomenon is attributed to Blank's significant (electro)chemical reactivity with Li metal, resulting in the swift depletion of the electrolyte with an associated increase in the viscosity of the electrolyte and the formation of an organic-rich SEI layer<sup>20, 21</sup>. Hence, 3-SN appeared to consume less electrolyte, particularly solvent, than the Blank. Moreover, before and after cycling, the interfacial resistance of 3-SN was lower than that of the Blank (**Fig. S9b**). This suggests that the nano-Si<sub>3</sub>N<sub>4</sub> additive effectively suppresses the (electro)chemical decomposition of the electrolyte, resulting in the formation of a thin, fast Li<sup>+</sup>-conductive SEI layer.



**Fig. S10.** (a) Modified Aurbach's Coulombic efficiency tests of 3 wt% of nitride additives in the Blank at 2 mA cm<sup>-2</sup>. (b) Enlargements of (a) for displaying nucleation overpotential. (c) Enlargements of (a) for displaying Coulombic efficiency. The particle size of nitrides are below 100 nm.

**Note)** In Fig. S10, various nanosized nitrides were tested; however, only nano-Si<sub>3</sub>N<sub>4</sub> improved the Coulombic efficiency. Hexagonal boron nitride (h-BN) has robust (electro)chemical inertness toward Li metal<sup>22</sup>; therefore, it might not possibly play a role in the formation of the nitride-based SEI layer through (electro)chemical decomposition. TiN and VN, unlike Si<sub>3</sub>N<sub>4</sub>, cannot form alloys with Li. Thus, it can be deduced that they have a limited capability to significantly decrease the nucleation overpotential or enhance the Coulombic efficiency. Furthermore, transition metal nitrides, in contrast to transition metal oxides, possess outstanding electrical conductivity<sup>23</sup>, thereby introducing the risk of short-circuit, as observed with VN.

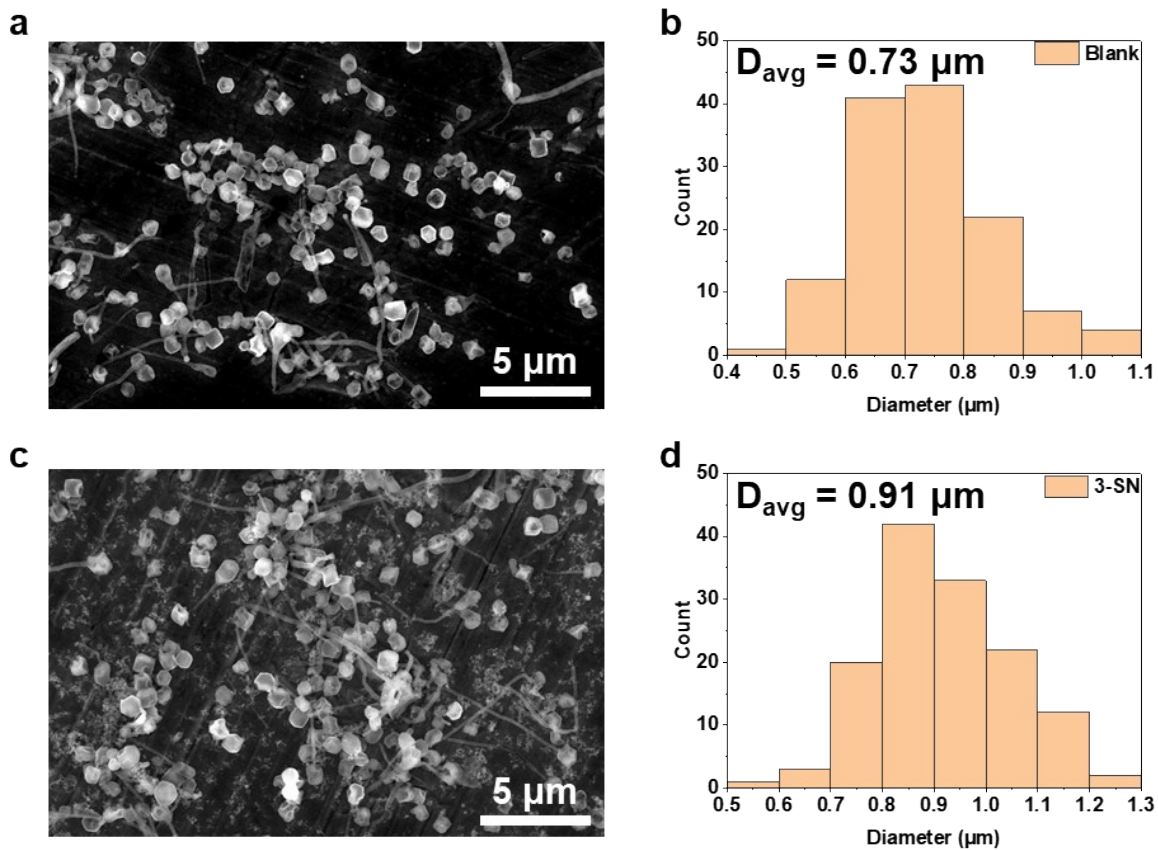
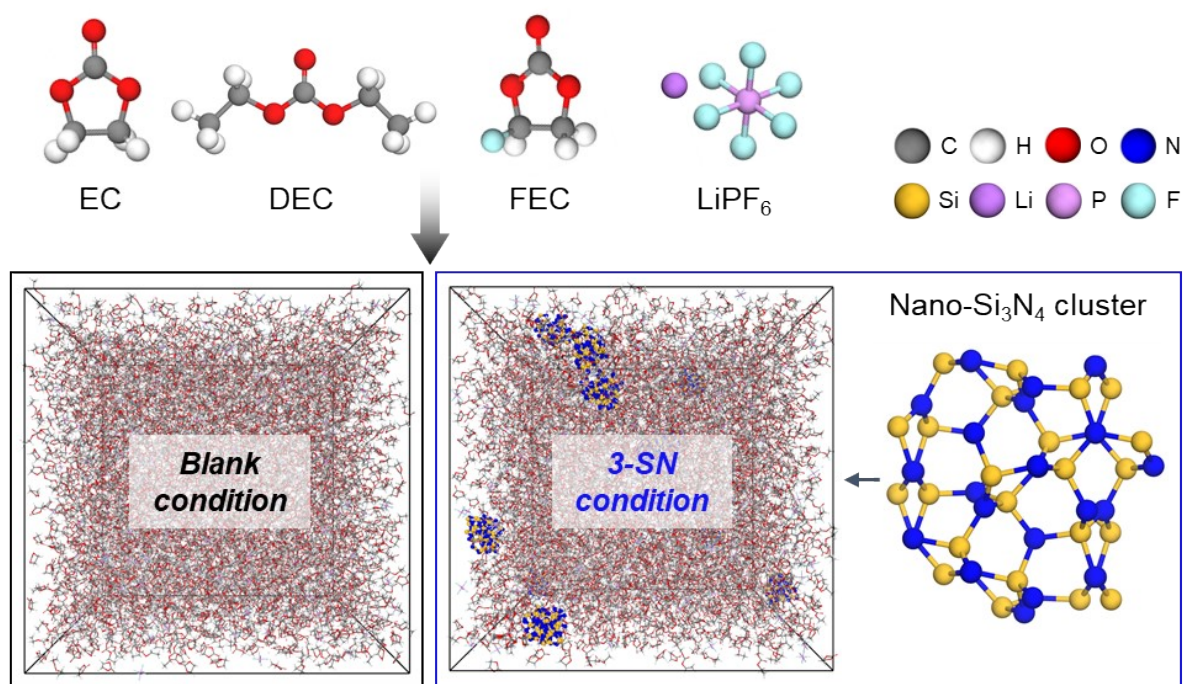


**Fig. S11.** Scanning electron microscope (SEM) images of Li nuclei after  $0.1 \text{ mA h cm}^{-2}$  of Li electrodeposition at  $0.5 \text{ mA cm}^{-2}$  in Li|Cu half-cell and histograms for their size. **(a), (b)** Blank. **(c), (d)** 3-SN.



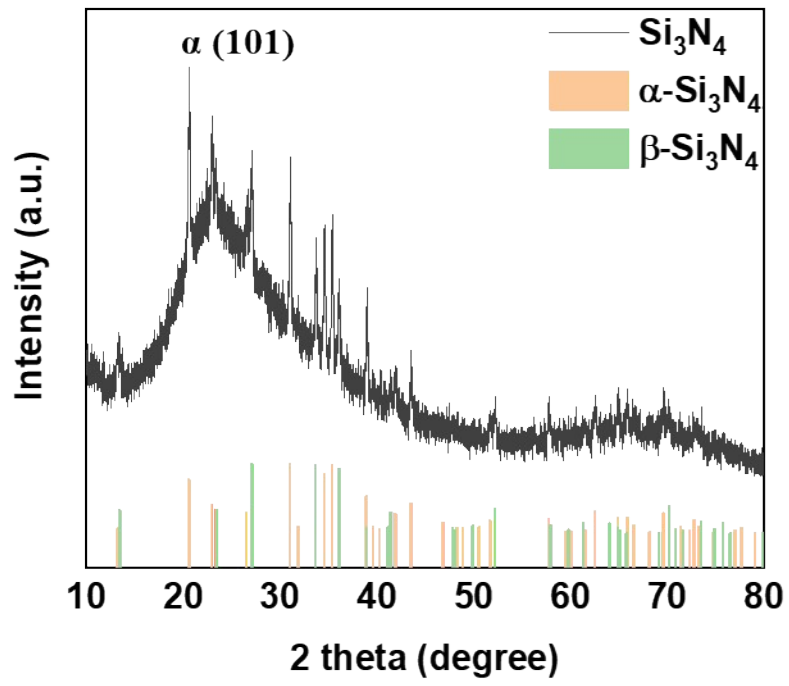
### **Blank condition**

1 M LiPF<sub>6</sub> EC/DEC (1:1 vol%) + 10 wt% FEC

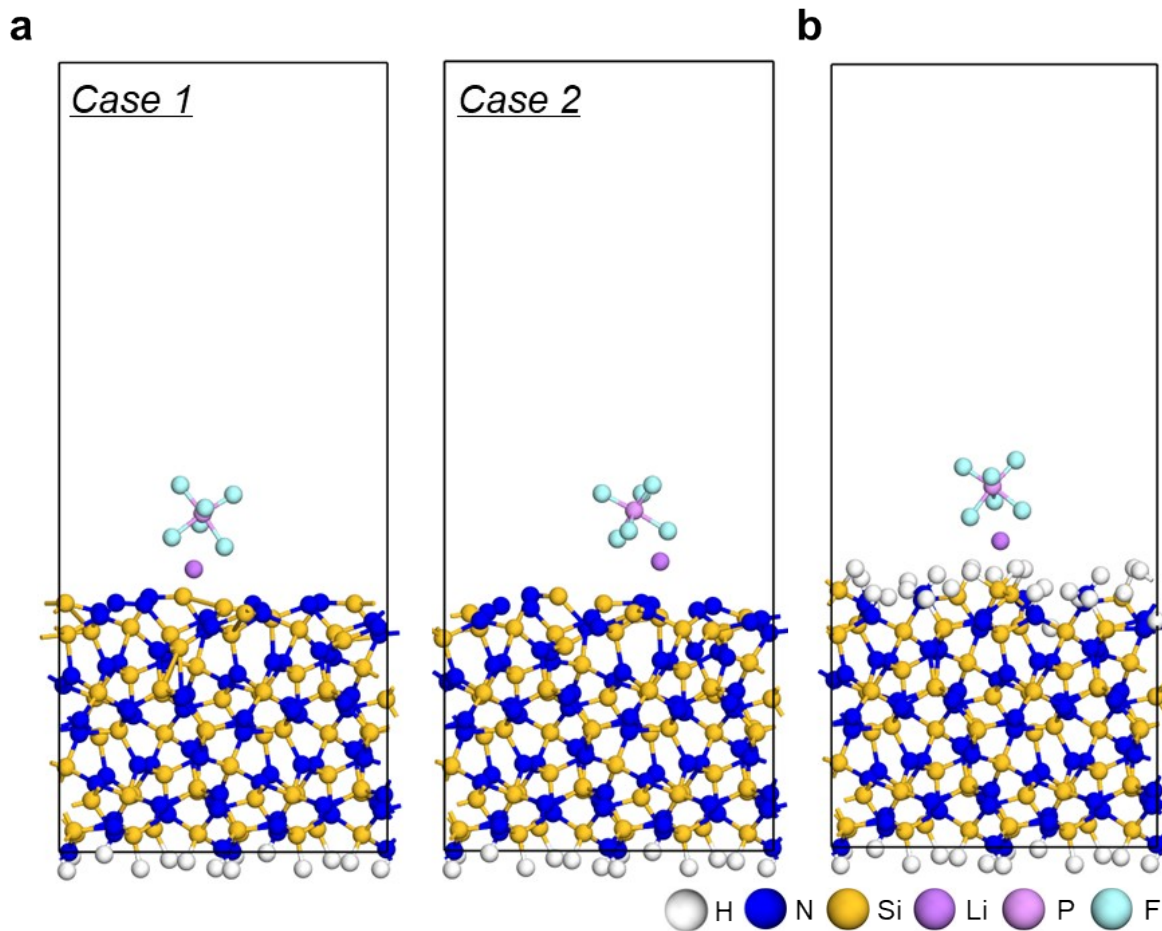
### **3-SN condition**

1 M LiPF<sub>6</sub> EC/DEC (1:1 vol%) + 10 wt% FEC + 3 wt% Si<sub>3</sub>N<sub>4</sub>

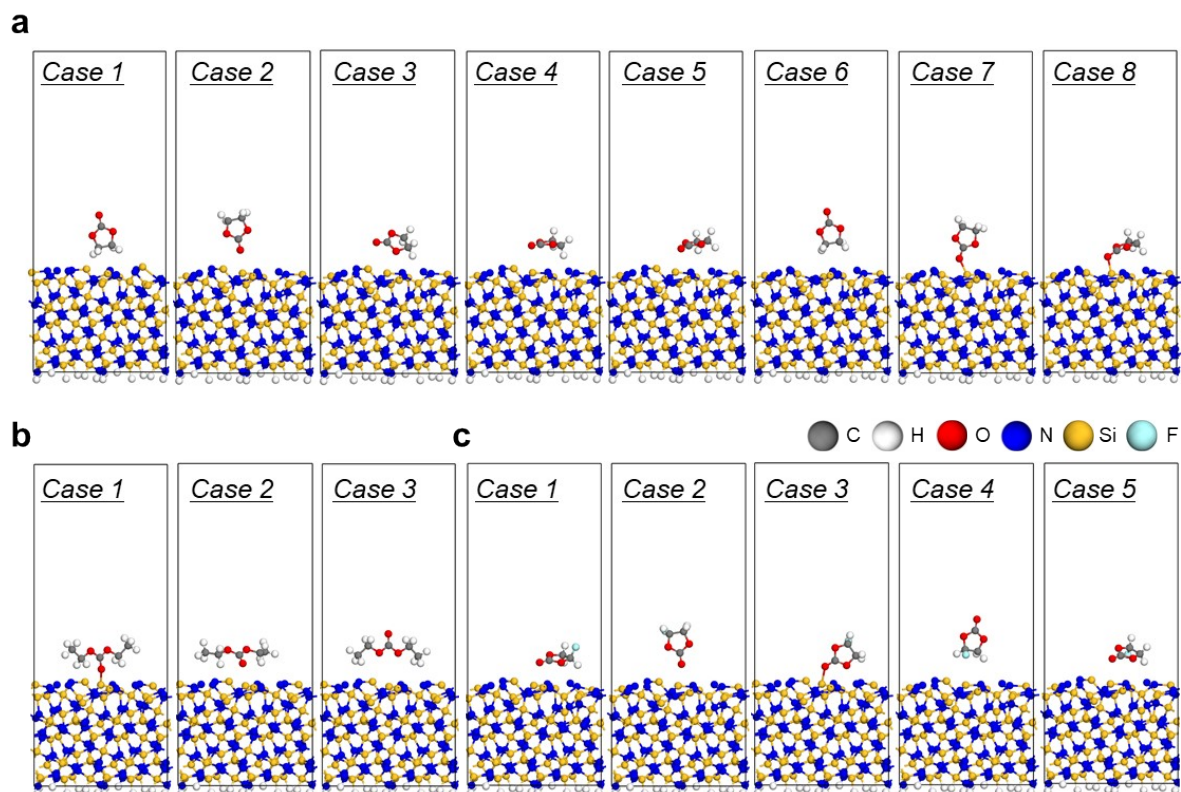
**Fig. S12.** Model systems for the molecular dynamics (MD) simulations (*i.e.*, Blank and 3-SN). In the electrolyte system of 3-SN, the nano-Si<sub>3</sub>N<sub>4</sub> cluster was composed by ten units of Si<sub>3</sub>N<sub>4</sub> (*i.e.*, (Si<sub>3</sub>N<sub>4</sub>)<sub>10</sub>). For the Blank, the number of EC, DEC, FEC, and LiPF<sub>6</sub> molecules are 2500, 1380, 470, and 340, respectively. For the 3-SN, the number of EC, DEC, FEC, LiPF<sub>6</sub>, and (Si<sub>3</sub>N<sub>4</sub>)<sub>10</sub> are 2500, 1380, 470, 340, and 11, respectively.



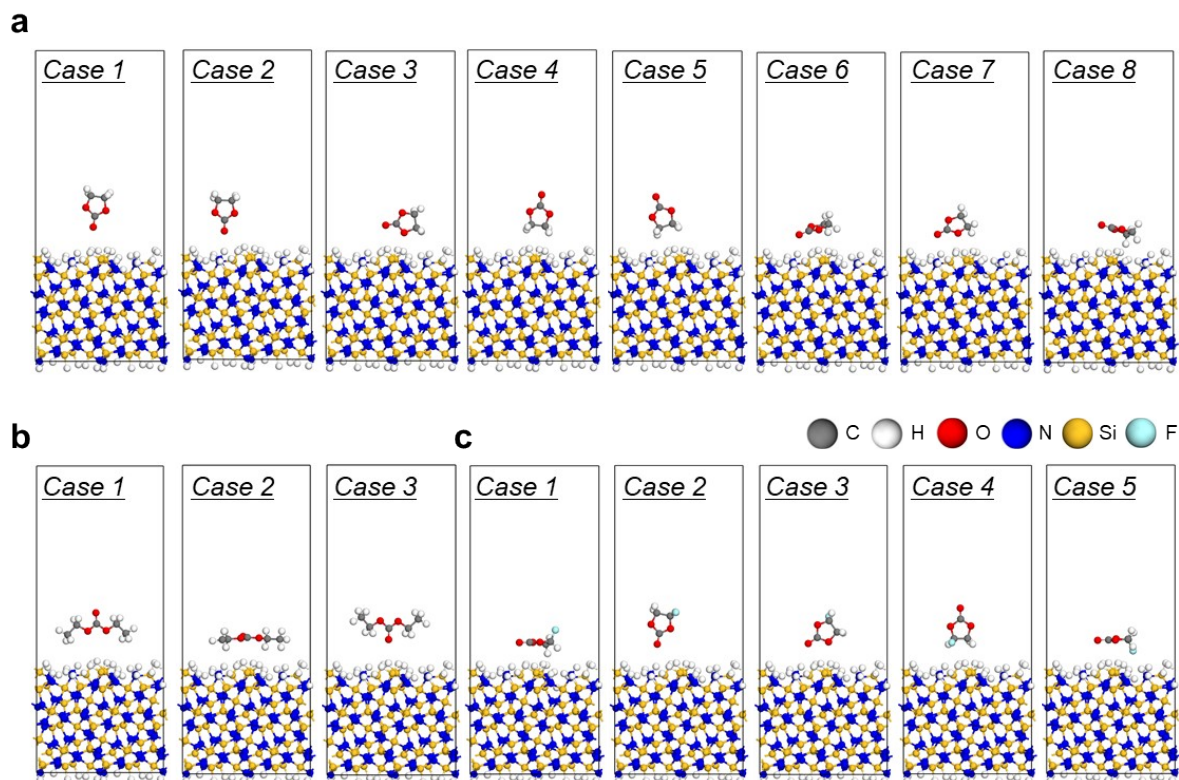
**Fig. S13.** X-ray diffraction (XRD) patterns of the nano-Si<sub>3</sub>N<sub>4</sub>



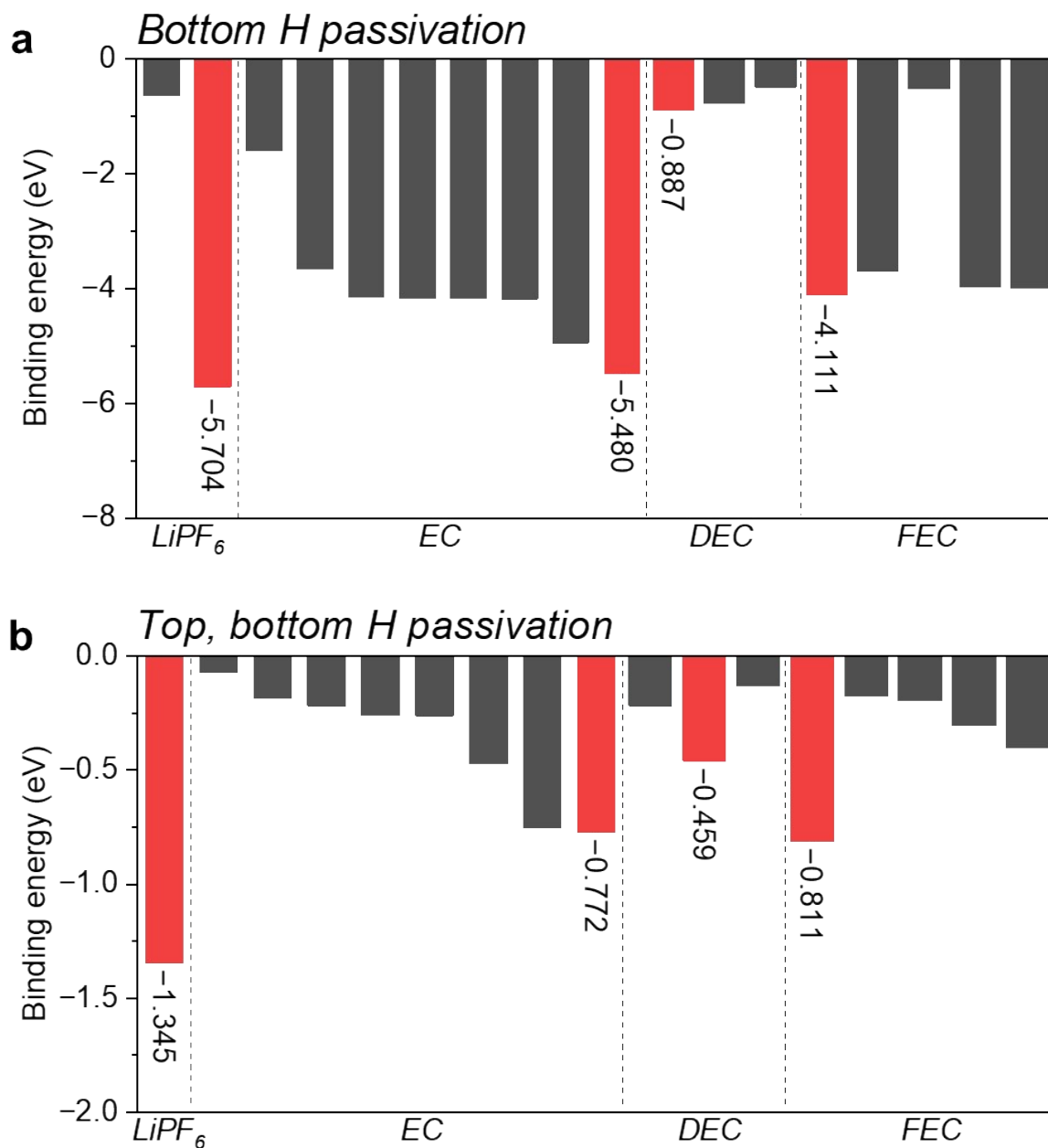
**Fig. S14.** Optimized structures of  $\text{LiPF}_6$  on the  $\alpha\text{-Si}_3\text{N}_4$  (101) surface. **(a)** Bottom H passivated surface. **(b)** Top and bottom H passivated surface. The various cases of  $\text{LiPF}_6$  configuration were considered. The surface of  $\text{Si}_3\text{N}_4$  consists of 161 atoms for the bottom H passivated surface and 187 atoms for the top and bottom H passivated surface. From the bottom side, 74 atoms are constrained. The vacuum spacing of model system is over 15 Å.



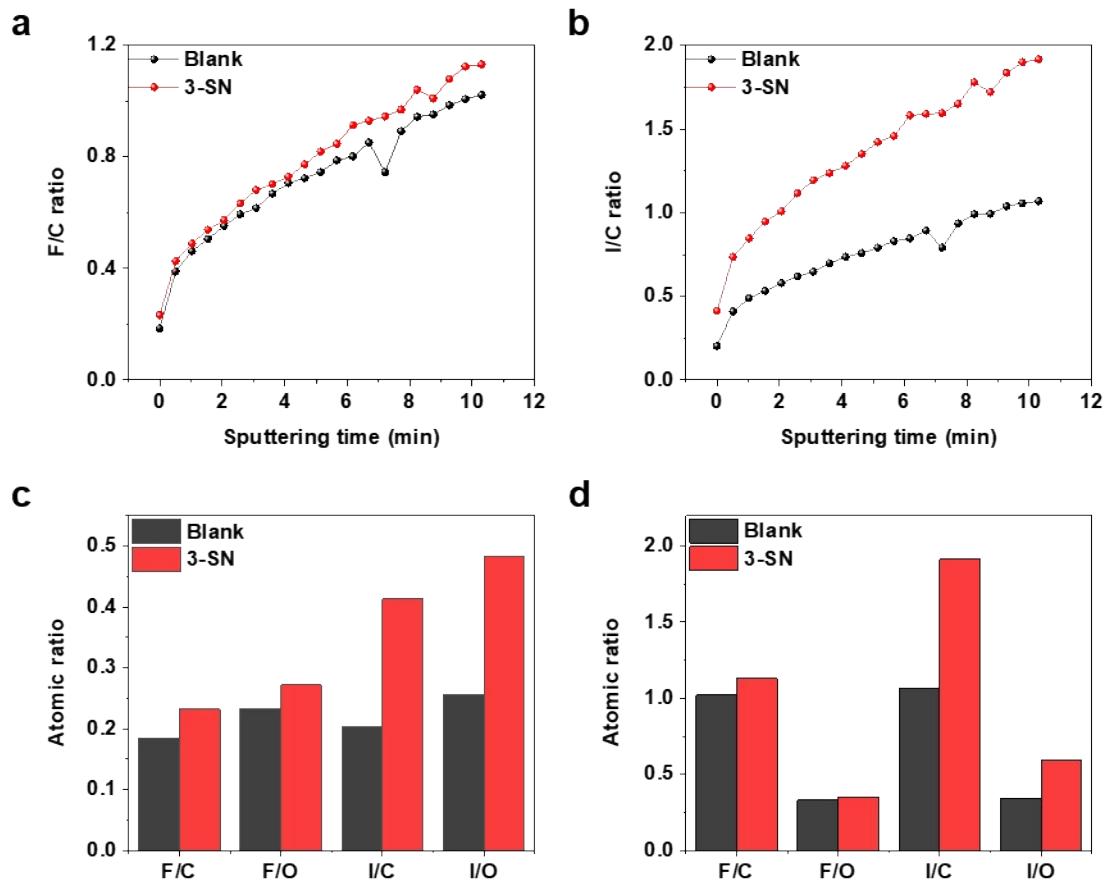
**Fig. S15.** Optimized structures of the electrolyte on the bottom H passivated  $\alpha$ - $\text{Si}_3\text{N}_4$  (101) surface. **(a)** EC, **(b)** DEC, and **(c)** FEC. The various cases of electrolyte configuration were considered. The surface of  $\text{Si}_3\text{N}_4$  consists of 161 atoms for the bottom H passivated surface and 187 atoms for the top and bottom H passivated surface. From the bottom side, 74 atoms are constrained. The vacuum spacing of model system is over 15 Å.



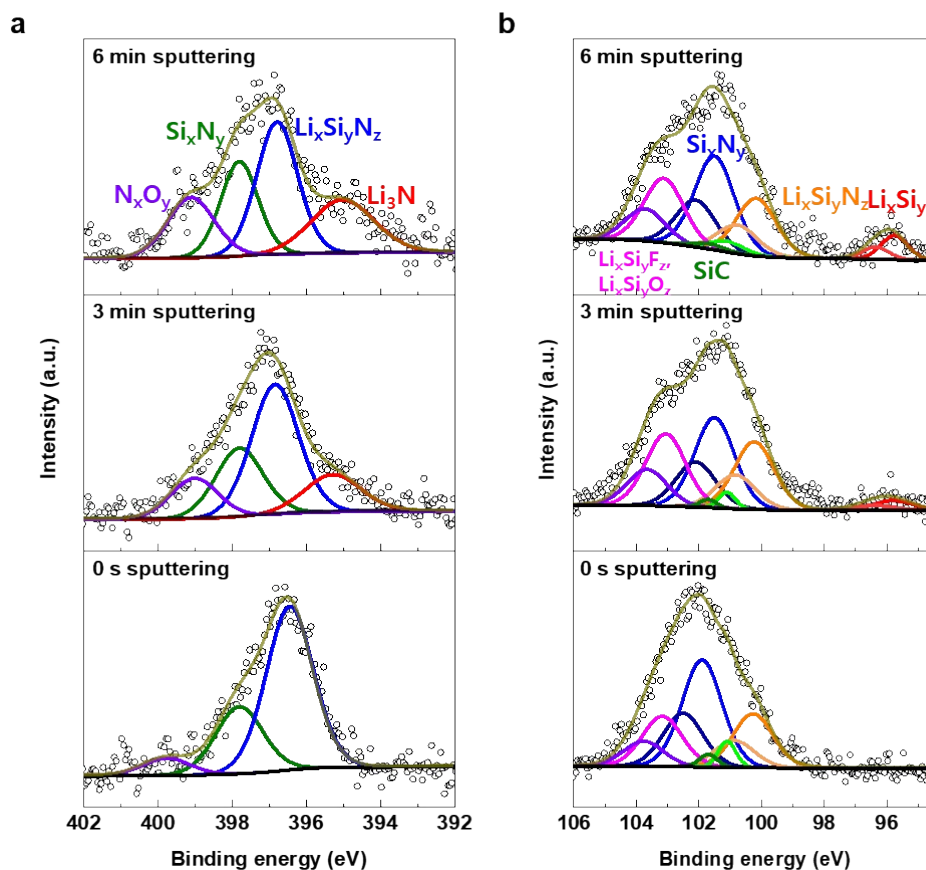
**Fig. S16.** Optimized structures of the electrolyte on the top and bottom H passivated  $\alpha$ - $\text{Si}_3\text{N}_4$  (101) surface. **(a)** EC, **(b)** DEC, and **(c)** FEC. The various cases of electrolyte configuration were considered. The surface of  $\text{Si}_3\text{N}_4$  consists of 161 atoms for the bottom H passivated surface and 187 atoms for the top and bottom H passivated surface. From the bottom side, 74 atoms are constrained. The vacuum spacing of model system is over 15 Å.



**Fig. S17.** Binding energies of  $\text{LiPF}_6$ , EC, DEC, and FEC on the  $\text{Si}_3\text{N}_4$  (101) surface. **(a)** Bottom H passivated  $\alpha$ - $\text{Si}_3\text{N}_4$  (101) surface and **(b)** top and bottom H passivated  $\alpha$ - $\text{Si}_3\text{N}_4$  (101) surface. The red bars indicate the lowest binding energies in each system.



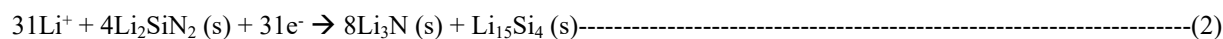
**Fig. S18.** XPS depth profiling results of Li/Li symmetric cell after 10 cycles under  $0.5 \text{ mA cm}^{-2}$  and  $1 \text{ mA h cm}^{-2}$ . **(a)** F/C ratio, **(b)** I (Inorganics, including F, P, Si, N)/C ratio, **(c)** atomic ratio before sputtering, **(d)** atomic ratio after 600s of Ar sputtering.



**Fig. S19.** XPS depth profiling results of 3-SN in LilCu half-cell after first deposition under  $0.5 \text{ mA cm}^{-2}$  and  $1 \text{ mA h cm}^{-2}$ . (a) N 1s XPS, (b) Si 2p XPS.

**Note)** Through an in-depth analysis of the TOF-SIMS and XPS depth profiling results (**Fig. 4** and **Fig. S19**), we propose a mechanism for the SEI layer formation facilitated by nano- $\text{Si}_3\text{N}_4$ . The N 1s XPS results indicate that the SEI layer was generated through the conversion and alloying reaction between nano- $\text{Si}_3\text{N}_4$  and Li metal (**Fig. S19a**). In addition, the lithiation and conversion reactions of nano- $\text{Si}_3\text{N}_4$  in close proximity to the Li metal exhibited a more pronounced effect. In the topmost SEI layer (0 s sputtering), the  $\text{Si}_3\text{N}_4$ :  $\text{Li}_x\text{Si}_y\text{N}_z$ :  $\text{Li}_3\text{N}$  ratio was 1.00:2.45:0. However, as it approached the Li metal (bottommost SEI layer, more sputtering), this ratio changes to 1.00:1.89:0.65, and further to 1.00:1.53:0.95. These changes indicate a higher presence of  $\text{Li}_3\text{N}$ , which is the final product of the conversion reaction. Furthermore, an increased presence of  $\text{Li}_x\text{Si}_y$  alloy is observed in the Si 2p XPS as it approaches the Li metal. This provides compelling evidence for the mechanism of SEI layer formation, primarily involving alloying and conversion reactions at the interface between nano- $\text{Si}_3\text{N}_4$  and Li metal (**Fig. S19b**).

Based on the TOF-SIMS, XPS, and cryo-TEM results, we propose the following as one of the possible mechanisms:



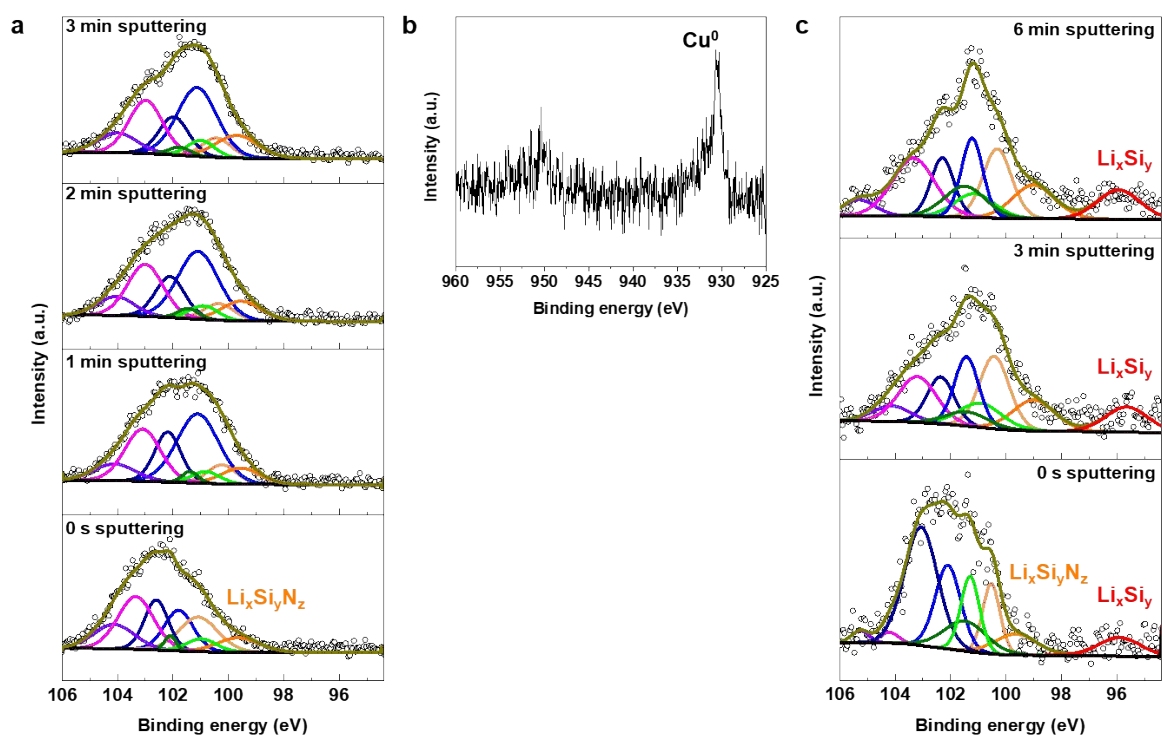


**Fig. S20.** XPS depth profiling results of 3-SN in a Li|Cu half-cell after cycling. **(a)** Si 2p XPS spectra after the first cycle. **(b)** Cu 2p XPS spectra after the first cycle. Since the thickness of the Li metal and SEI layer after the first cycle (following Li stripping) is significantly reduced compared to that after Li deposition,  $\text{Cu}^0$  appears after 3 minutes of sputtering. **(c)** Si 2p XPS spectra after subsequent Li deposition. The Si 2p XPS spectra confirm the reversibility of alloying reaction between Li metal and nano- $\text{Si}_3\text{N}_4$ . However, the  $\text{Li}_x\text{Si}_y\text{N}_z$  peak persisted throughout cycling, indicating that delithiation of  $\text{Li}_x\text{Si}_y\text{N}_z$  did not occur.

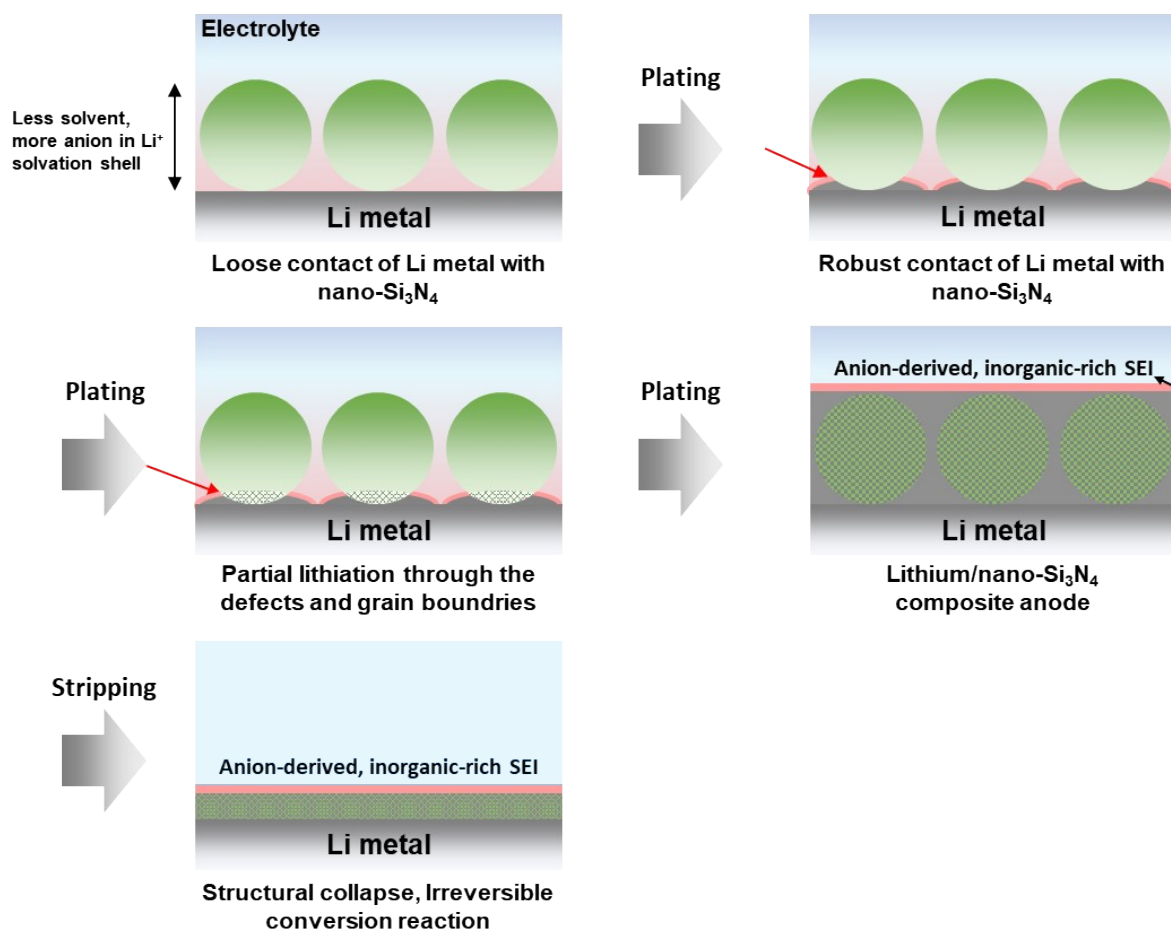
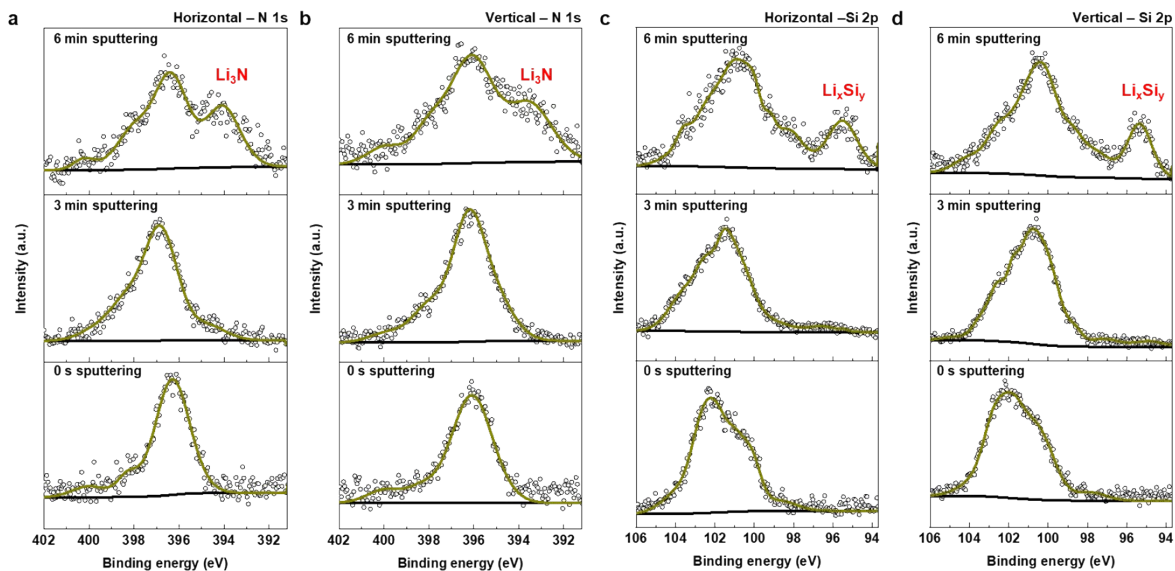
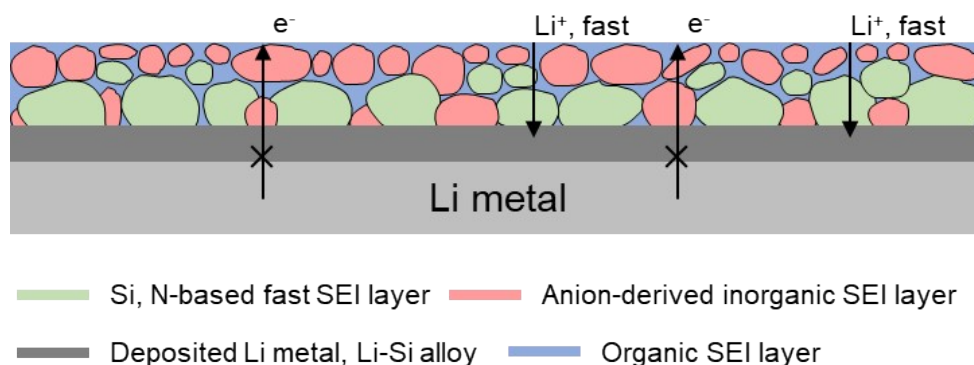


Fig. S21. Proposed mechanisms of the SEI layer formation facilitated by  $\text{nano-Si}_3\text{N}_4$  reaction with Li metal.



**Fig. S22.** Effect of the orientation of the cell: XPS depth profiling results of 3-SN in Li||Li symmetric-cell after first deposition under  $0.5 \text{ mA cm}^{-2}$  and  $1 \text{ mA h cm}^{-2}$ . **(a)** N 1s XPS for the horizontal cell, **(b)** N 1s XPS for the vertical cell, **(c)** Si 2p XPS in horizontal cell, **(d)** Si 2p XPS in vertical cell.

**Note)** A comparison of the N 1s and Si 2p XPS spectra for both orientations revealed no significant differences. Notably, a distinctive  $\text{Li}_x\text{Si}_y$  peak was observed at 6 minutes of sputtering (inner SEI layer) in both orientations, confirming the alloy reaction between Li metal and nano- $\text{Si}_3\text{N}_4$ . Furthermore, the inner SEI was found to contain a higher proportion of  $\text{Li}_3\text{N}$ , the final product of the conversion reaction. These findings provide compelling evidence that both cell orientations experienced the same alloying and conversion reactions between nano- $\text{Si}_3\text{N}_4$  and Li metal for SEI formation mechanism.



**Fig. S23.** Schematic representation of the SEI layer formed by 3-SN.

**Note)** Supported by **Fig. 4**, **Fig. S19-S22**, we propose that the inner SEI layer mainly consists of  $\text{Li}_x\text{Si}_y\text{N}_z$  and  $\text{Li}_3\text{N}$ -based fast  $\text{Li}^+$ -conductive SEI, whereas the outer SEI layer is predominantly composed of anion-derived inorganic-rich SEI. The formation of an organic SEI layer originating from the electrolyte solvents was significantly suppressed by the modulation of the  $\text{Li}^+$  solvation environment. The bi-layered structure of the SEI layer formed by 3-SN can enhance the cycle life of Li metal for several reasons.

**Firstly**, nano- $\text{Si}_3\text{N}_4$  derived Si,N-based SEI layer, provides a fast  $\text{Li}^+$  conductive pathway, facilitating fast interfacial kinetics and promoting spherical Li metal growth. While the conventional LiF-rich SEI layer suffers from poor  $\text{Li}^+$  conductivity (LiF,  $\text{Li}^+$  conductivity:  $\sim 10^{-31}$ )<sup>24</sup>, both the inner SEI layer and the intermittent organic SEI layer offer much better  $\text{Li}^+$  conductive pathways. **Secondly**, the LiF-rich anion-derived SEI layer possessed superior mechanical strength (Young's modulus of LiF: 64.97 GPa), effectively suppressing Li dendrite growth. **Thirdly**, the LiF-rich outer SEI layer prevents electron transfer from the electrode to the electrolyte owing to its high bandgap (8.9 eV). Although  $\text{Li}_3\text{N}$  is susceptible to electron tunneling owing to its poor bandgap (1.1 eV)<sup>24</sup>, the outer LiF-rich SEI layer can effectively prevent electron tunneling. **Lastly**, the organic SEI layer easily dissolves in the electrolyte, exposing Li metal to the electrolyte and further decomposing the electrolyte. Moreover, SEI layer swelling increases the contact between the SEI layer and Li metal, exacerbating electrolyte decomposition. However, 3-SN generates a less organic but more inorganic-based SEI layer, mitigating SEI layer dissolution and swelling, resulting in a higher Coulombic efficiency and greater tolerance to chemical corrosion<sup>1</sup> (**detailed in Fig. S24**).

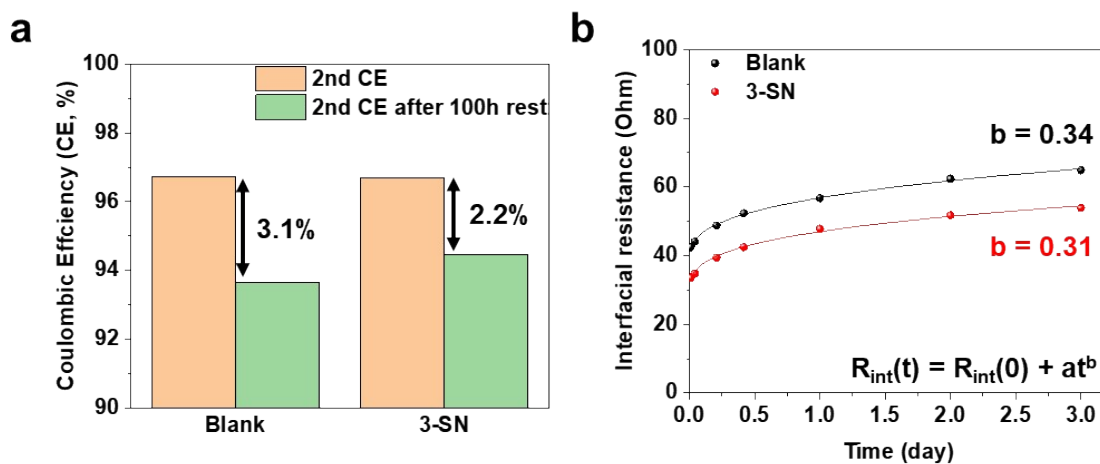


**Fig. S24.** (a) Coulombic efficiency difference of the second cycle between 0 h rest and 100 h rest after 4 mA h cm<sup>-2</sup> deposition under 2 mA cm<sup>-2</sup> in Li|Cu half-cell, (b) Measured  $R_{int}(t)$  from EIS during periodic rest in a Li|Li symmetric cell, and corresponding non-linear least squares fit to a power law.

**Note)** As confirmed by the EIS results (**Fig. S9**), the  $R_{SEI}$  of 3-SN before cycling is markedly lower than that of the Blank. Hence, 3-SN is less vulnerable to chemical corrosion, which occurs via a chemical reaction between the electrolyte and Li metal during calendar aging<sup>1</sup>. **Fig. S24a** reflects both the effects of the morphology of the electrodeposited Li metal (*i.e.* surface area) and the intrinsic susceptibility of the electrolyte on chemical corrosion. Based on the cryo-TEM and FIB-SEM images (**Fig. 4**), it was observed that 3-SN promoted the formation of comparatively dense and spherical Li deposits, whereas the Blank resulted in dendritic Li deposits. Given that spherical Li electrodeposits possess a lower surface area, 3-SN results in a diminished disparity in Coulombic efficiency between periods of rest and non-rest conditions. In contrast, **Fig. S24b** shows the intrinsic susceptibility of the electrolyte to chemical corrosion. The initial  $R_{SEI}$  and its growth over time ( $b$  value in power law) were both greater for the Blank, signifying that the accumulation of the SEI layer resulting from chemical corrosion was more pronounced than that of 3-SN<sup>1</sup>.

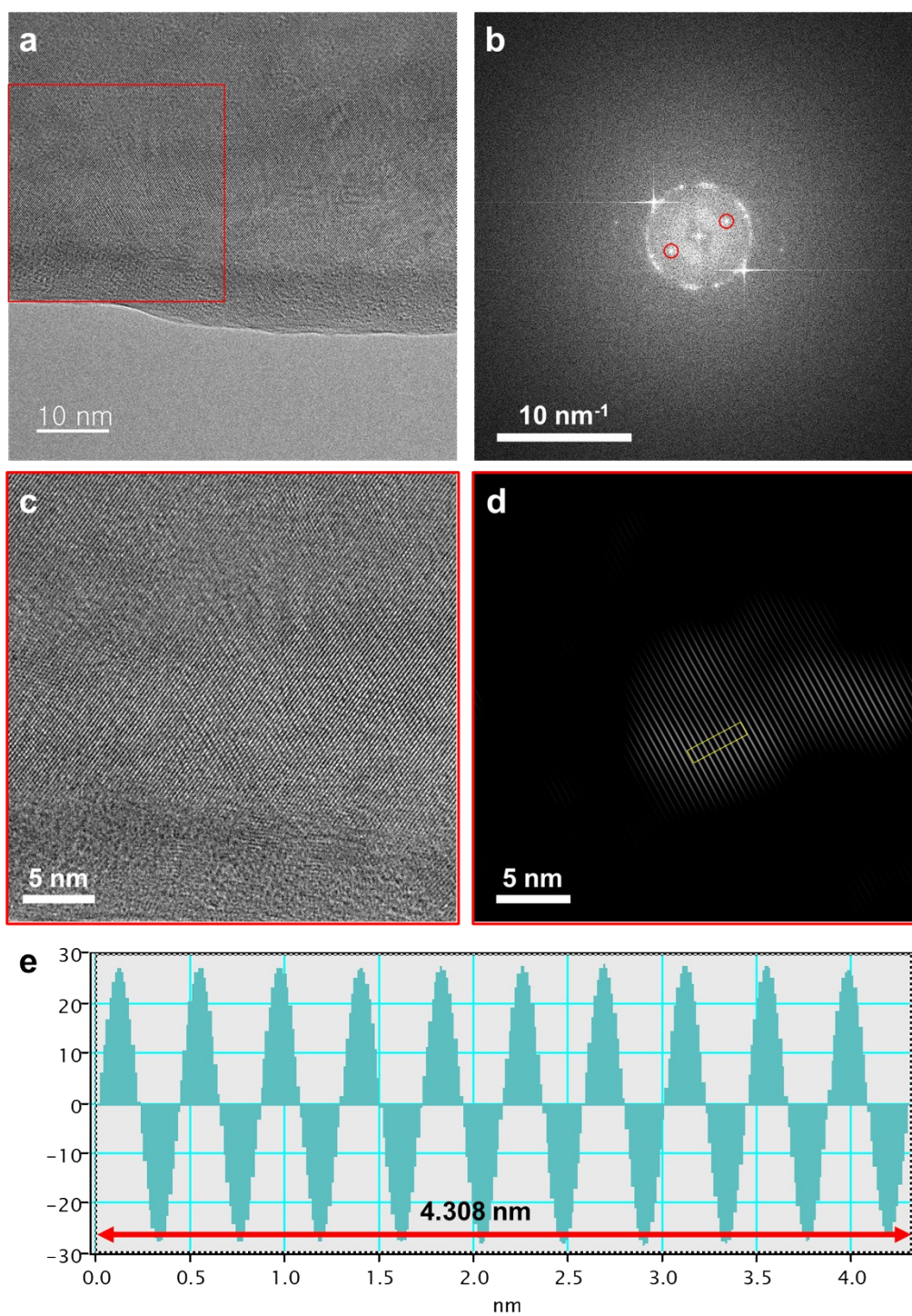


**Fig. S25.** In-depth analysis of the Cryo-TEM results in **Fig. 4f**. **(a)** Selected area for HRTEM analysis. **(b)** FFT patterns from the selected area, presumed to correspond to Li-Si alloy. **(c)** Enlarged view of the selected area in **Fig. S25a**. **(d)** Inverse FFT of **Fig. S25c**. **(e)** Profile of the Inverse FFT corresponding to the yellow box in **Fig. S25d**. The calculated d-spacing value closely matches that of the  $\text{Li}_{15}\text{Si}_4$  (211) plane<sup>3</sup>, falling within the margin of error (**Table S8**).

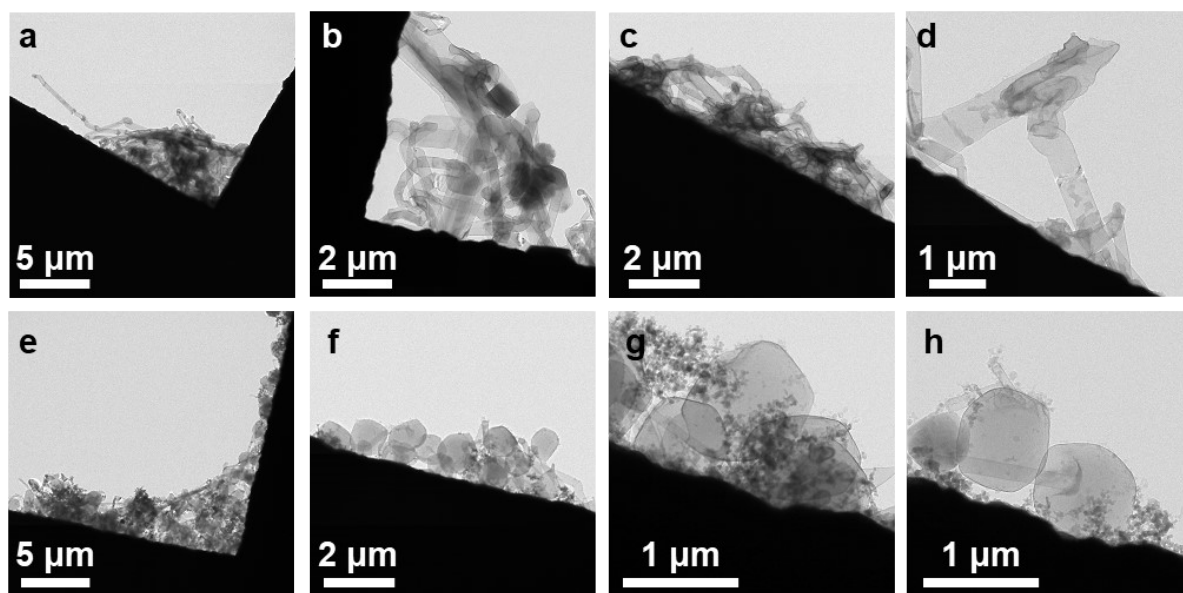


**Fig. S26.** Cryo-TEM images of Li deposition morphology under  $0.5 \text{ mA cm}^{-2}$  and  $0.17 \text{ mA h cm}^{-2}$ . **(a)-(d)** Blank, **(e)-(h)** 3-SN.

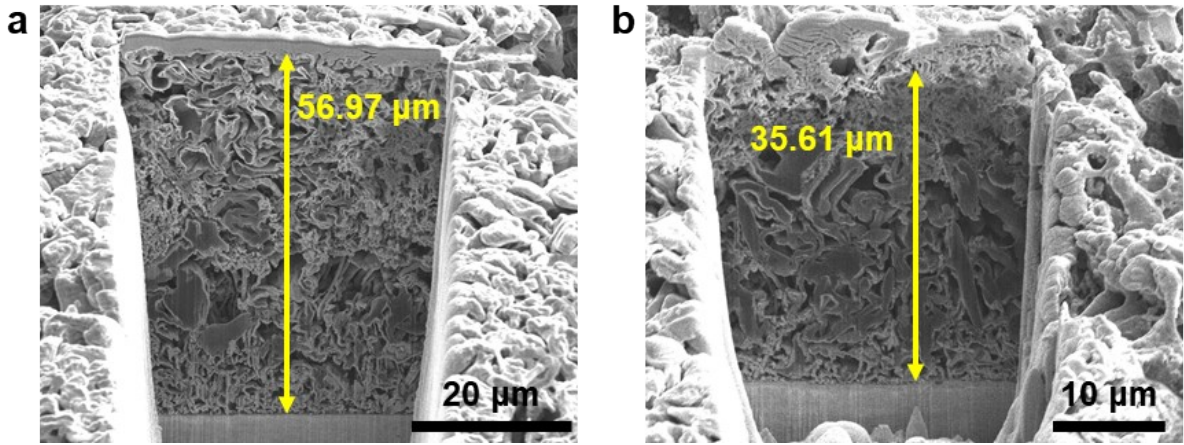


**Fig. S27.** Cross-sectional FIB-SEM images after 4 mA h cm<sup>-2</sup> of Li deposition on Cu foil under 2 mA cm<sup>-2</sup>. The theoretical thickness of Li is 20 μm. **(a)** Blank, **(b)** 3-SN.

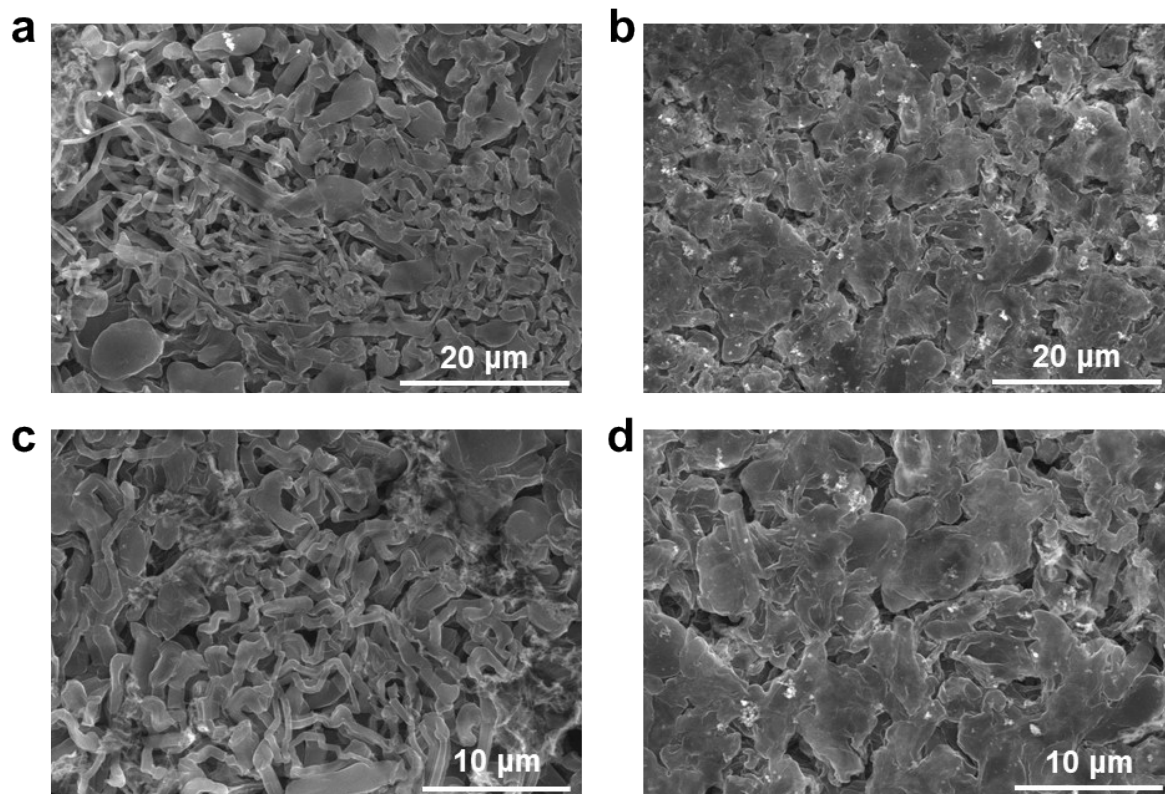


**Fig. S28.** SEM images of Li deposits ( $2 \text{ mA h cm}^{-2}$ ) on Cu foil under  $0.5 \text{ mA cm}^{-2}$ . **(a), (c)** Blank, **(b), (d)** 3-SN.

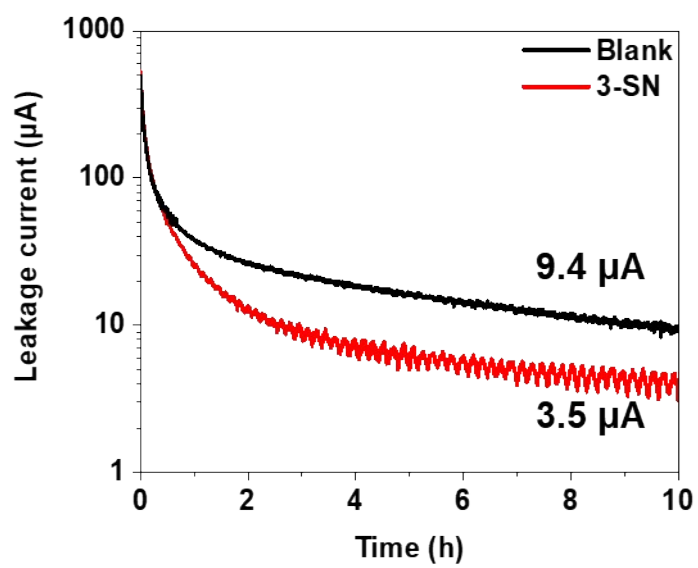


**Fig. S29.** Chronoamperometry results at 4.5V vs. Li/Li<sup>+</sup> of Li|NCM811 full-cell.

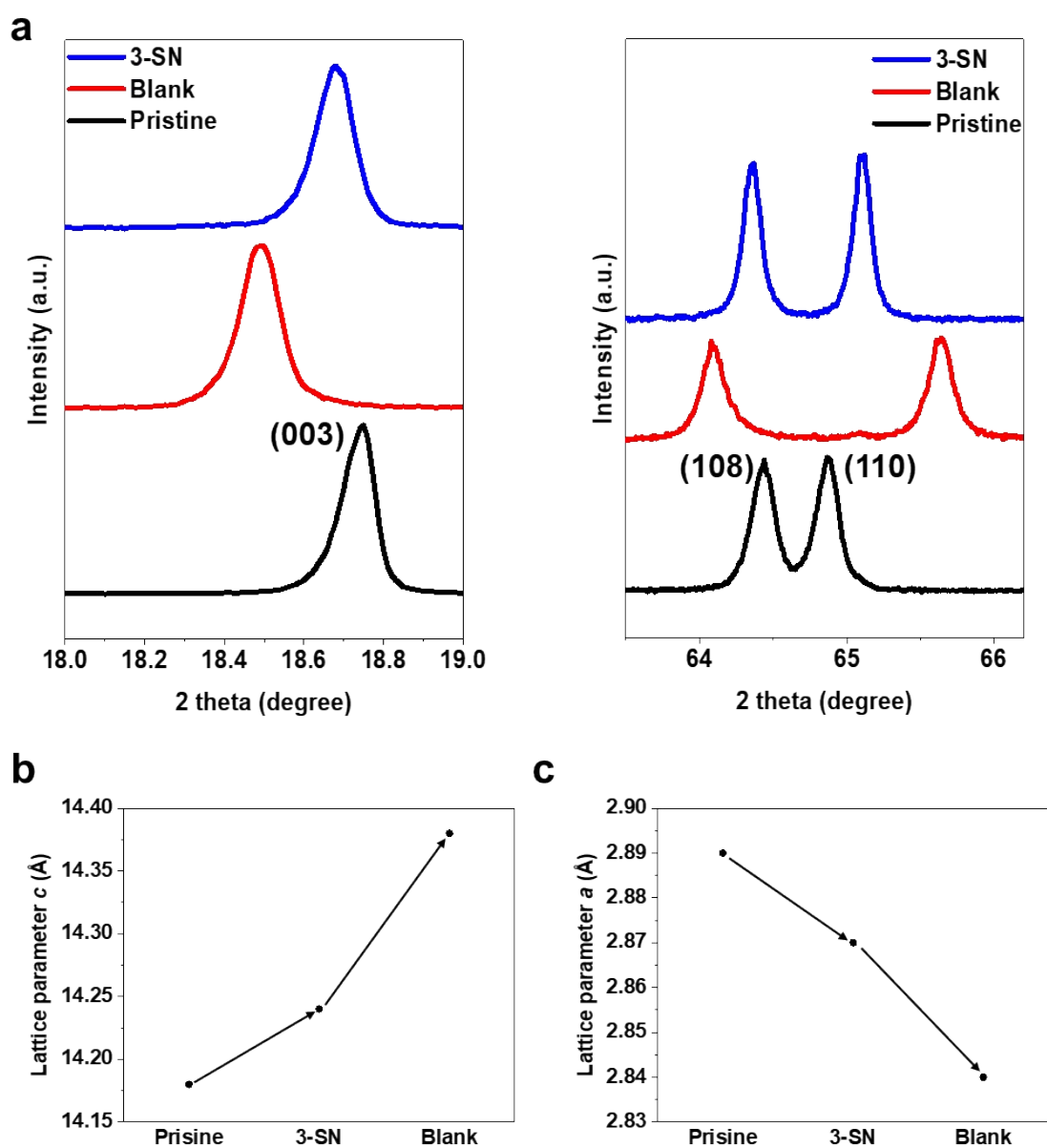


**Fig. S30.** (a) XRD patterns of NCM811 after 50 cycles under 4.5-3.0V and 0.5C, 1D. (b), (c) Changes in lattice parameters of NCM811 after cycling. The lattice parameters were calculated based on the relationship between the interplanar spacing of the (003) and (108) planes and the lattice parameters of the hexagonal system (NCM811, R-3m). More pronounced shifts in the lattice parameters are associated with reduced Li content, resulting from irreversible side reactions such as electrolyte oxidation decomposition, cation mixing, oxygen loss, and transition metal dissolution.

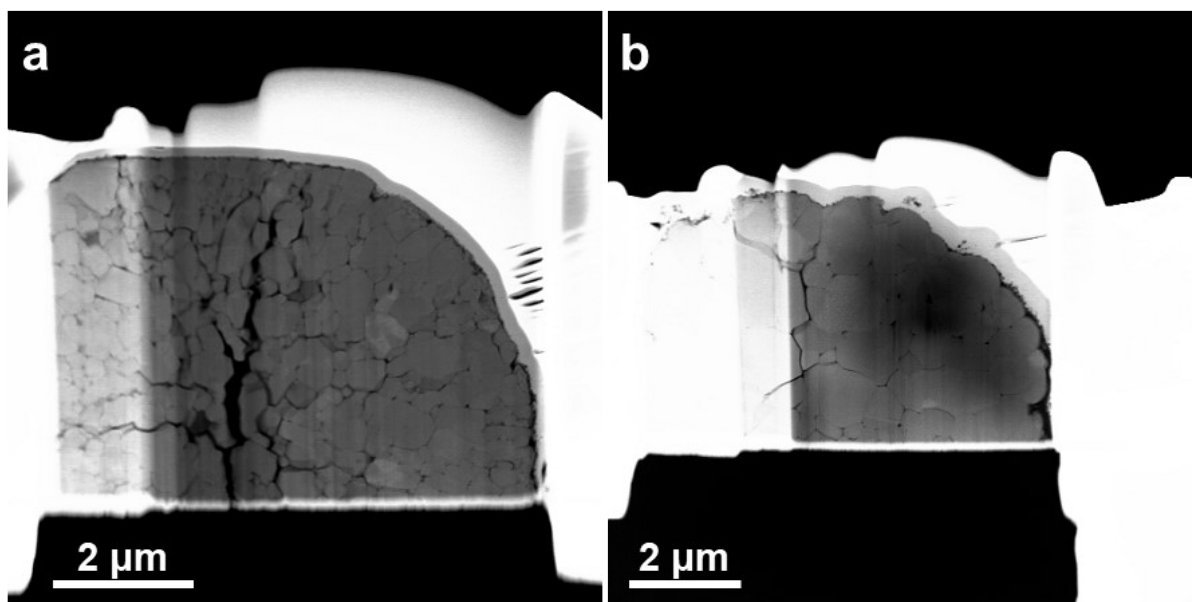


**Fig. S31.** TEM cross-sectional images of NCM811 retrieved from Li||NCM811 after 50 cycles under 4.5-3.0V and 0.5C, 1D. **(a)** Blank, **(b)** 3-SN.

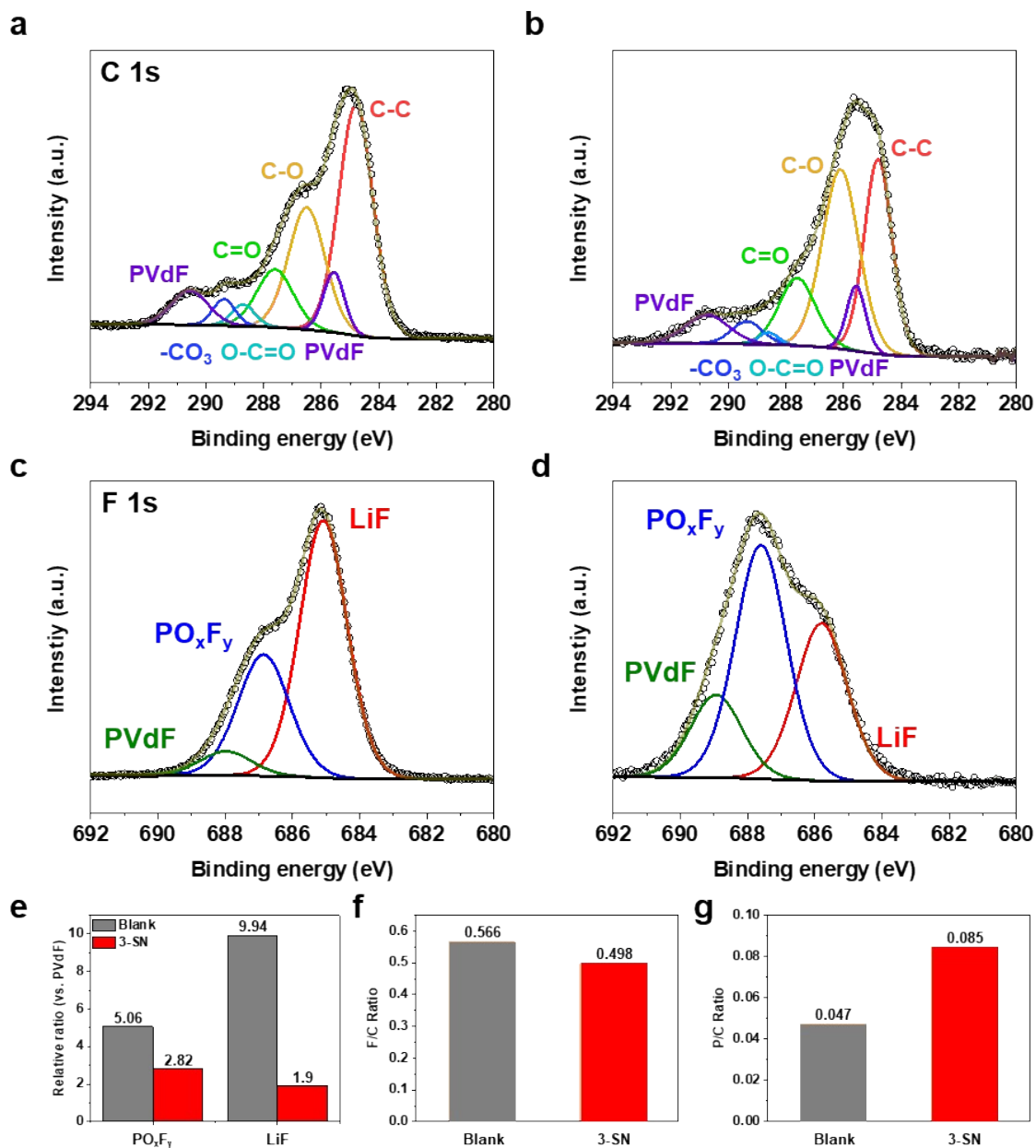


**Fig. S32.** XPS results of NCM811 retrieved from Li||NCM811 after 50 cycles under 4.5-3.0V and 0.5C/1D. **(a)**, **(c)** Blank, **(b)**, **(d)** 3-SN, **(e)-(g)** Relative ratio and atomic ratio, originated from XPS results.

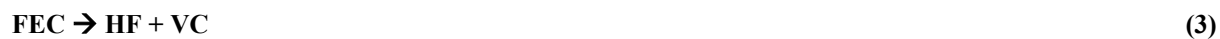
**Note)** Following high-voltage cycling, the C 1s spectrum of the CEI layer showed no significant differences (**Fig. S32a, b**); however, noticeable differences were observed in the F 1s spectrum (**Fig. S32c, d**). As confirmed by the HRTEM results (**Fig. 5e**), the F 1s spectrum confirmed that the CEI layer formed by the Blank contained a significant quantity of LiF and minimal polyvinylidene fluoride (PVDF), suggesting the existence of a thick CEI layer (**Fig. S32e**). LiPF<sub>6</sub>-based electrolytes produce HF during cycling because of the thermal decomposition and hydrolysis of LiPF<sub>6</sub>. Additionally, at high temperatures, fluoroethylene carbonate (FEC) is susceptible to the attack of Lewis acids, resulting in the formation of HF and vinylene carbonate (VC; dehydrofluorination of FEC)<sup>25</sup>. HF is extremely corrosive and can cause damage to the CEI and SEI layers as well as to anodes and cathodes. The P/C ratio, which can be formed from LiPF<sub>6</sub>, is higher for 3-SN, whereas the F/C ratio is higher for the Blank (**Fig.**

**S32f, g).** This indicates that the CEI layer of the Blank was significantly fluorinated by the HF generated during cycling, whereas the HF in the 3-SN was removed by nano-Si<sub>3</sub>N<sub>4</sub>.

**The decomposition mechanisms of LiPF<sub>6</sub> are below;**



**The dehydrofluorination mechanism of FEC is below;**



**The fluorination mechanisms of CEI layer are below;**



Damage to the CEI layer caused by HF is progressively exacerbated by the H<sub>2</sub>O byproduct.

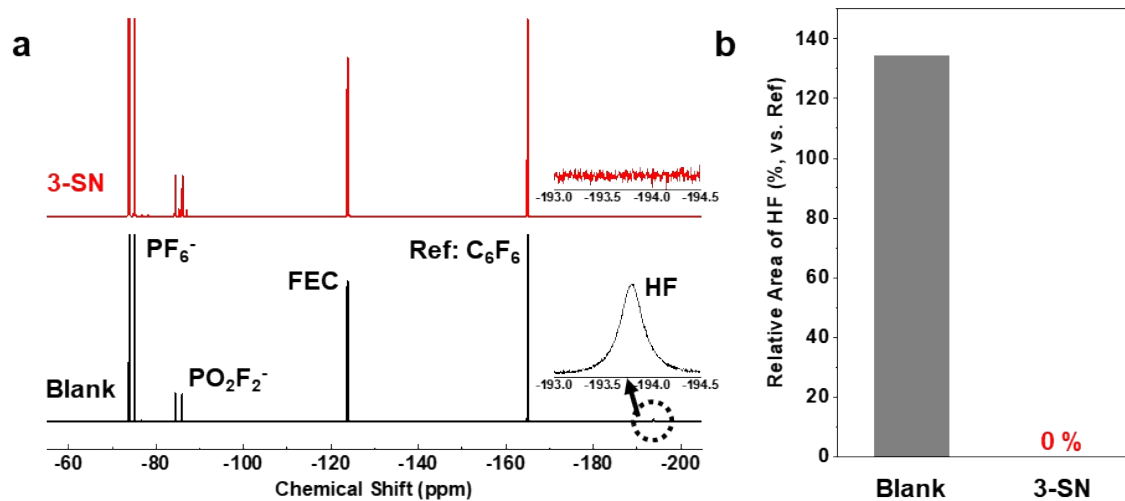


**Fig. S33.** (a)  $^{19}\text{F}$  NMR results of electrolytes after 7 days of storage at 60 °C. (b) Relative area of HF vs. Reference ( $\text{C}_6\text{F}_6$ ).

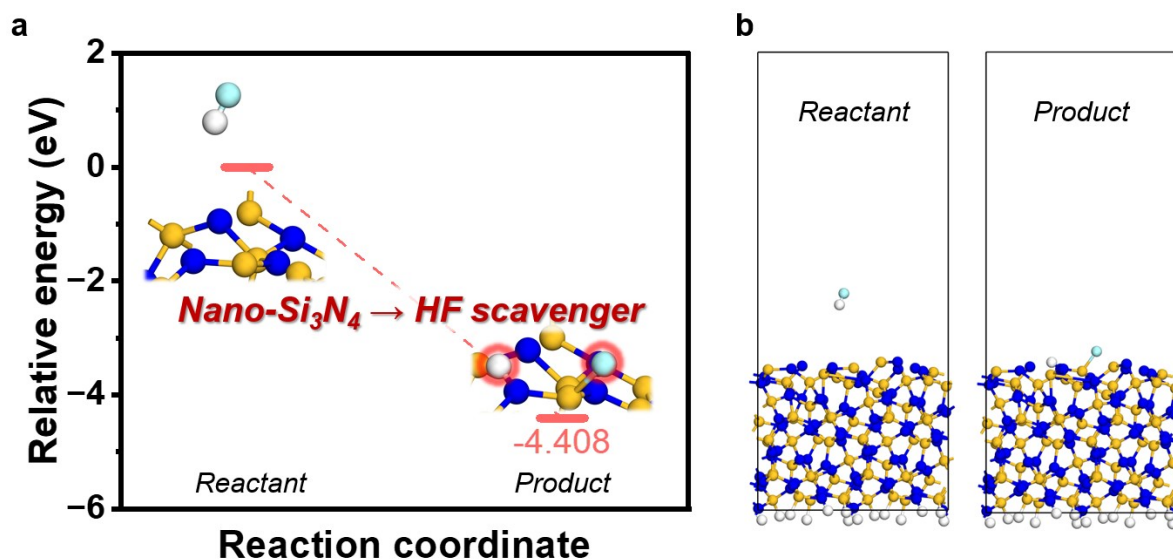


**Fig. S34.** (a) Reaction of HF scavenging on  $\alpha$ - $\text{Si}_3\text{N}_4$  (101) surface. (b) Optimized structures in the reaction of HF scavenging on the bottom H passivated  $\alpha$ - $\text{Si}_3\text{N}_4$  (101) surface.

**Note)** To further validate the HF scavenging mechanism, we performed the density functional theory (DFT) calculations to investigate the reaction between HF and the  $\alpha$ - $\text{Si}_3\text{N}_4$  (101) surface. Our DFT results revealed that the reaction of HF with the  $\alpha$ - $\text{Si}_3\text{N}_4$  (101) surface is thermodynamically favorable (*i.e.*, exothermic reaction), with a significantly negative relative energy between the reactant and product of approximately -4.41 eV (**Fig. S34a**). Notably, the reaction between nano- $\text{Si}_3\text{N}_4$  and HF leads to the formation of stable Si-F and N-H bonds, suggesting that nano- $\text{Si}_3\text{N}_4$  drives HF scavenging mechanism.

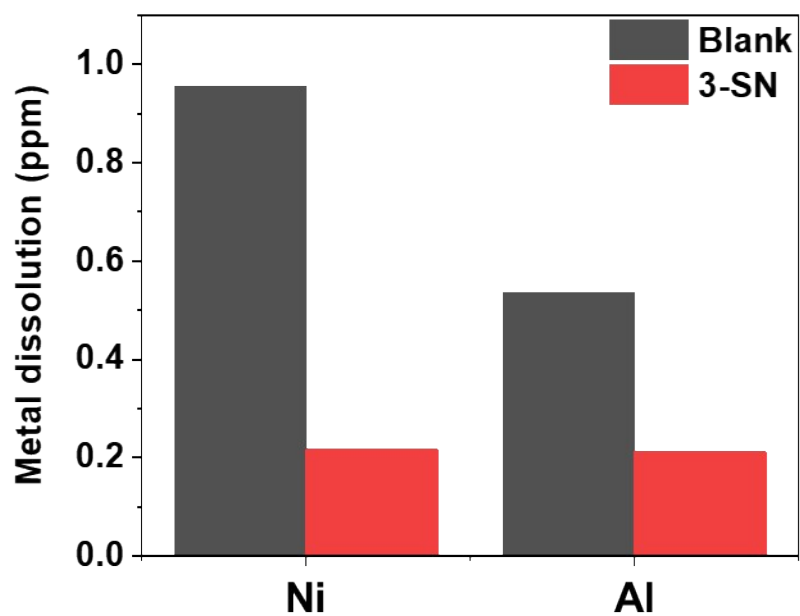


**Fig. S35.** Inductively coupled plasma mass spectrometer (ICP-MS) results of  $\text{Ni}^{2+}$  and  $\text{Al}^{3+}$  dissolution. Cathodes were retrieved from  $\text{Li}||\text{NCM811}$  after 4.5V vs.  $\text{Li}/\text{Li}^+$  charging, followed by 60°C storage in electrolytes for 3 days. The resulting electrolyte was then conducted to ICP-MS analysis.

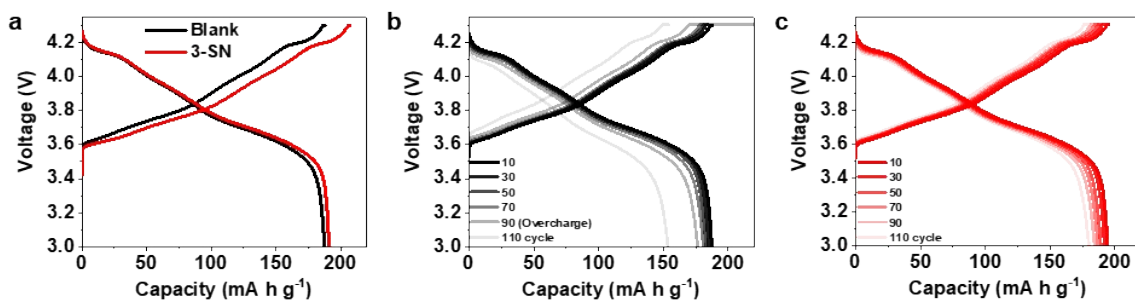


**Fig. S36.** Voltage profiles for **Fig. 6a**. **(a)** Voltage profiles for the first cycle. **(b)** Voltage profiles for the Blank. **(c)** Voltage profiles for 3-SN. The charging/discharging overpotential of the Blank is higher than 3-SN, even at the first cycle. The Blank experienced overcharging at the 90<sup>th</sup> cycle, followed by rapid cell degradation. The overcharge originated from the oxidation decomposition of the electrolyte and the deterioration of the cathode and CEI layer.

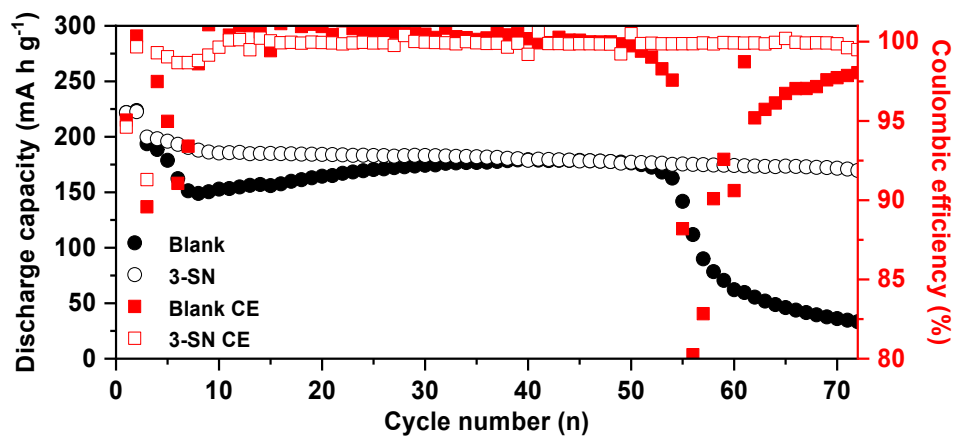


**Fig. S37.** Electrochemical test results of Li||NCM811 full-cell under high-voltage and high-rate. N/P = 10 (200  $\mu\text{m}$  Li || 3.8 mA h cm<sup>-2</sup> NCM 811), E/C = 12  $\mu\text{L}$  mAh<sup>-1</sup>, 4.5-3.0V, 1C/1D

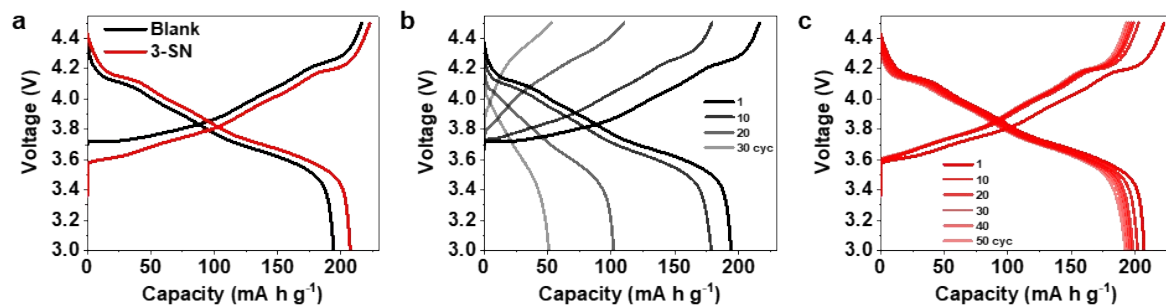


**Fig. S38.** Voltage profiles for **Fig. 6b**. **(a)** Voltage profiles for the first cycle. **(b)** Voltage profiles for the Blank. **(c)** Voltage profiles for 3-SN. Similar to **Fig. S36**, but a more dramatic results are observed in **Fig. S38**.

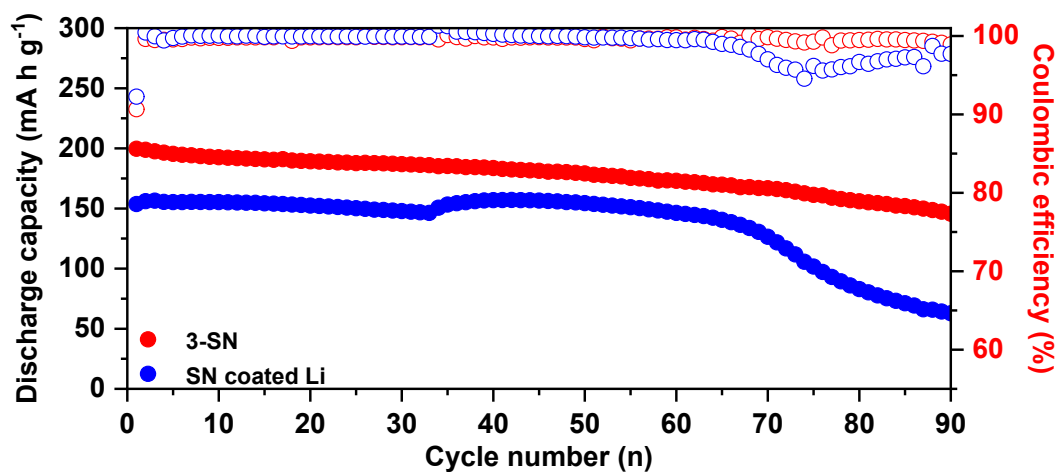


**Fig. S39.** Electrochemical test results of the Li||NCM811 full-cell with nano-Si<sub>3</sub>N<sub>4</sub> coated Li (SN-coated Li). N/P = 2.5 (50 μm Li || 3.8 mA h cm<sup>-2</sup> NCM 811), E/C = 4 μL mAh<sup>-1</sup>, 0.5C/1D, 4.5-3.0V.

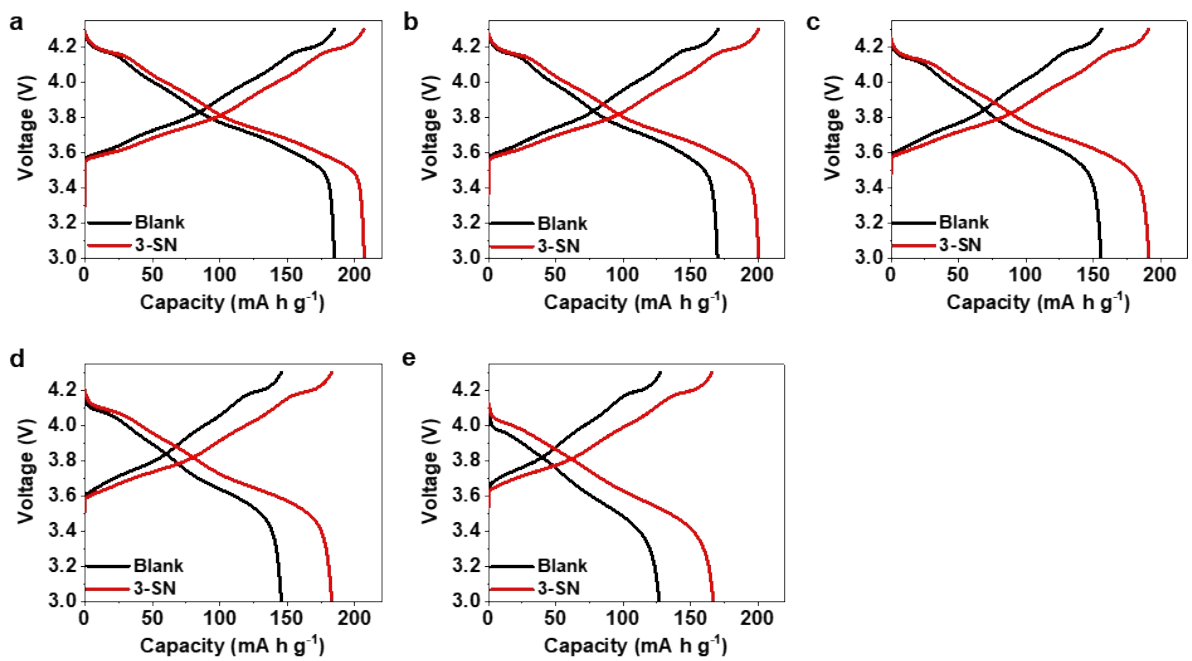


**Fig. S40.** Voltage profiles for the last 5<sup>th</sup> cycles at each C-rate in Fig. 6c. (a) 0.1C/0.1D. (b) 0.1C/0.2D. (c) 0.1C/0.5D. (d) 0.1C/1D, (e) 0.1C/2D.

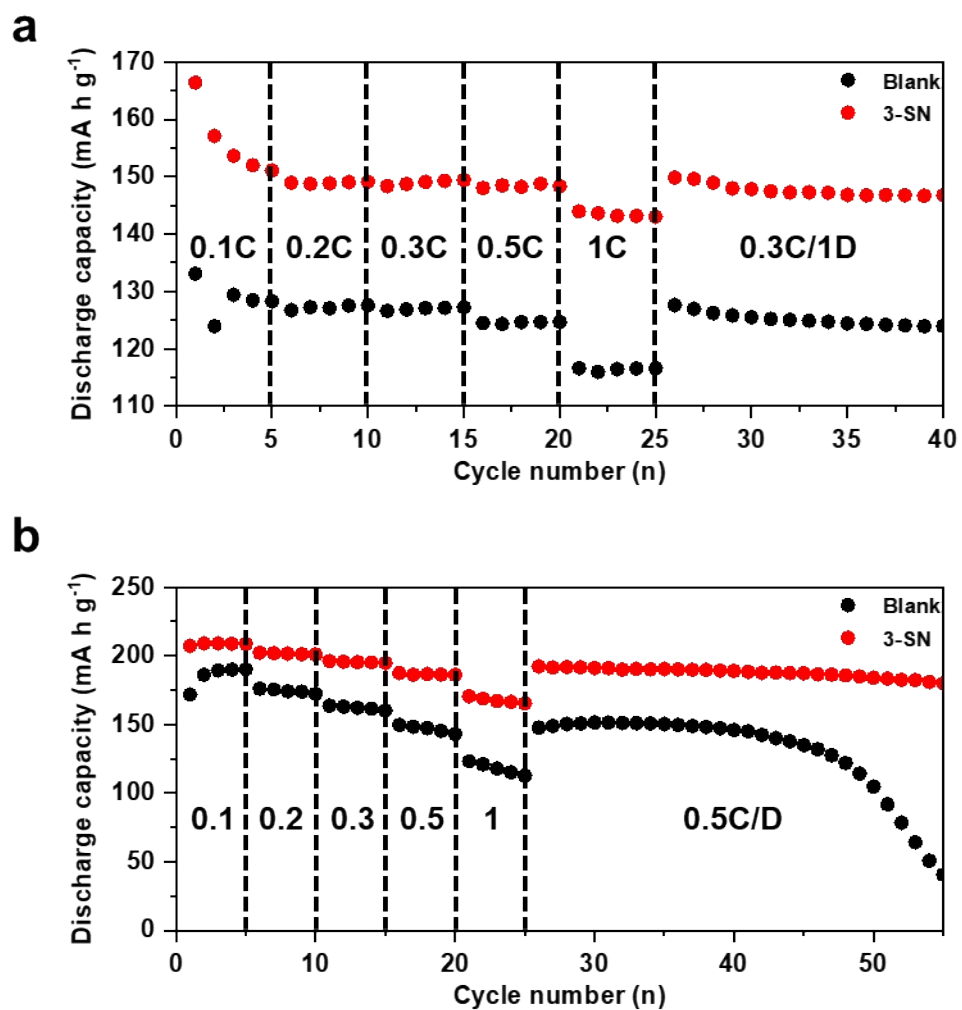


**Fig. S41.** Rate test results of Li||NCM811 full-cell. N/P = 2.5 (50  $\mu$ m Li || 3.8 mA h cm<sup>-2</sup> NCM 811), E/C = 4  $\mu$ L mAh<sup>-1</sup>, 4.3-3.0V, without CC/CV charging. **(a)** Asymmetric operation with constant discharging C-rate of 1D, **(b)** Symmetric charging/discharging C-rate operation.

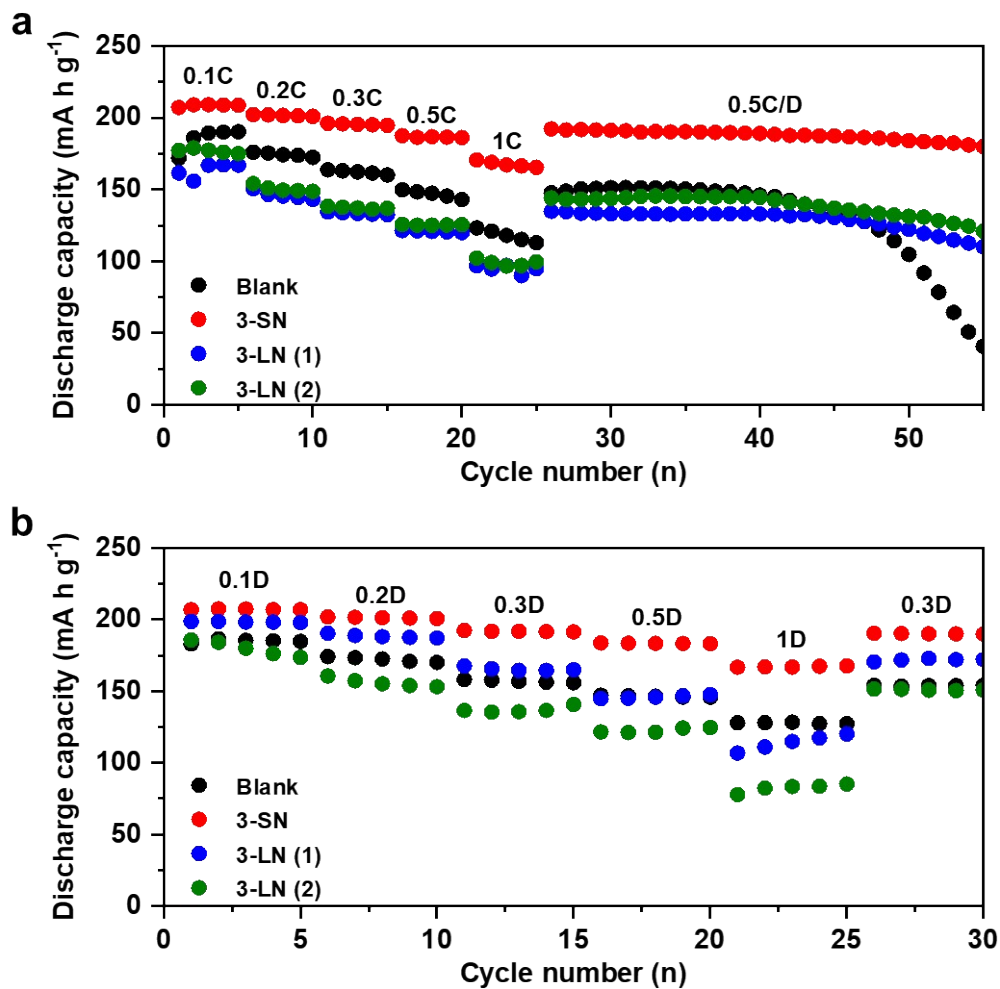


**Fig. S42.** Rate test results of Li||NCM811 full-cell. N/P = 2.5 (50  $\mu\text{m}$  Li || 3.8 mA h cm<sup>-2</sup> NCM 811), E/C = 4  $\mu\text{L}$  mAh<sup>-1</sup>, 4.3-3.0V, without CC/CV charging. The 3-LN, as previously reported, refers to 3 wt% of nano-Li<sub>3</sub>N in the Blank. **(a)** Symmetric charging/discharging C-rate operation. **(b)** Asymmetric operation with constant charging C-rate of 0.1C.

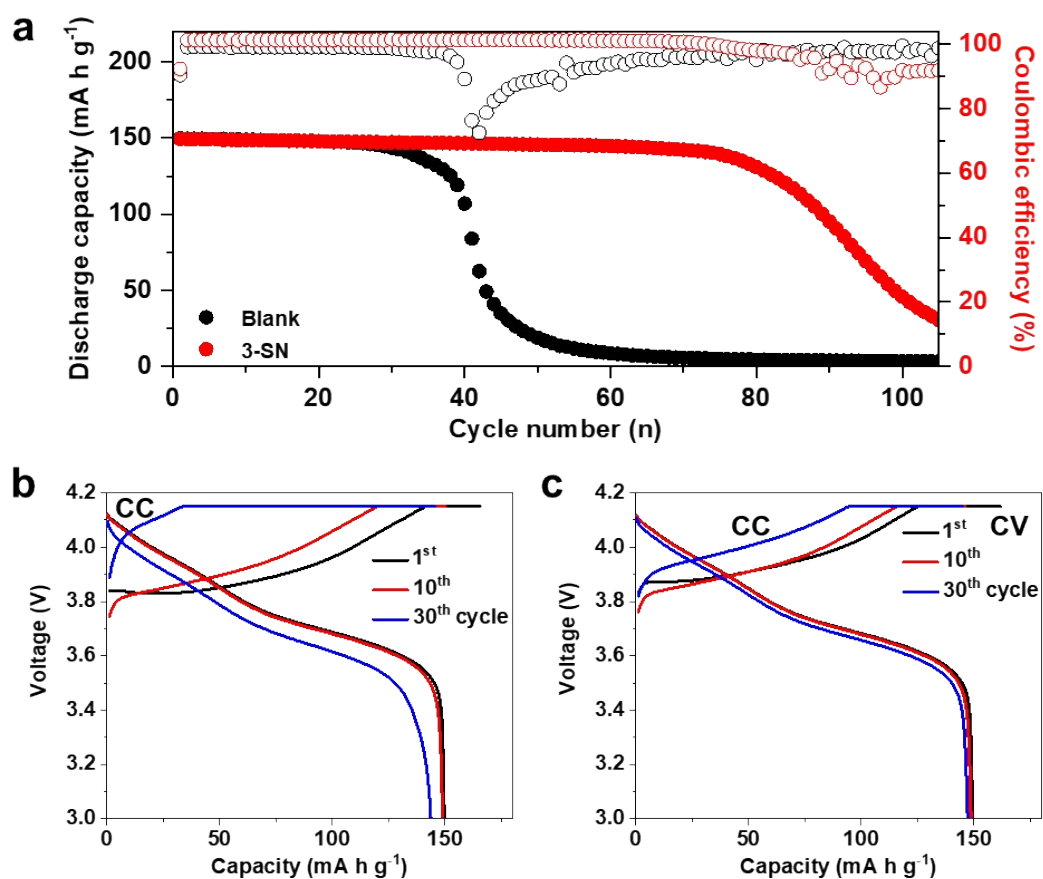


**Fig. S43.** (a) Electrochemical test results of Li||NCM811 full-cell under the fast-charging protocol (4C charging/1D discharging). (b) Voltage profiles of the Blank electrolyte. (c) Voltage profiles of the 3-SN electrolyte. The areal capacity of NCM811 was 2.4 mAh cm<sup>-2</sup>, with 50  $\mu$ L of electrolyte injected. The charging cut-off voltage for the fast-charging protocol was limited to 4.15 V to mitigate oxidative degradation during the constant-voltage (CV) charging process. The constant current (CC) charging region for the Blank shortened much more rapidly than that of the 3-SN, owing to the increased internal resistance of the full-cell.

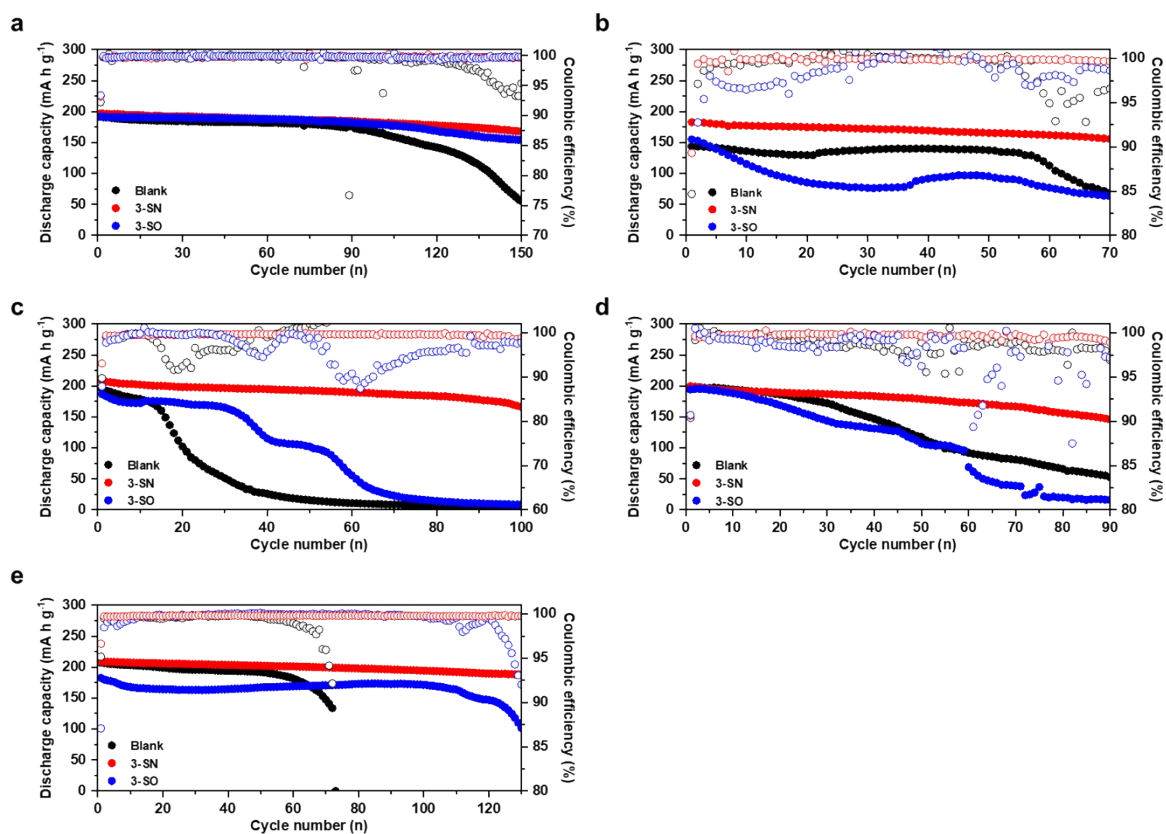


**Fig. S44.** Electrochemical test results of Li||NCM811 full-cell. 3 wt% of nano-silica in the Blank is denoted as 3-SO. N/P = 2.5 (50  $\mu\text{m}$  Li || 3.8 mA h cm<sup>-2</sup> NCM 811), E/C = 4  $\mu\text{L}$  mAh<sup>-1</sup>. **(a)** 4.3-3.0V, 0.2C/0.5D (CC/CV: 0.05C). **(b)** 4.3-3.0V, 0.5C/1D. **(c)** 4.5-3.0V, 0.2C/0.5D. **(d)** 4.5-3.0V, 0.5C/1D. **(e)** 4.3-3.0V, 0.2C/0.5D (CC/CV: 0.05C), 50 °C.

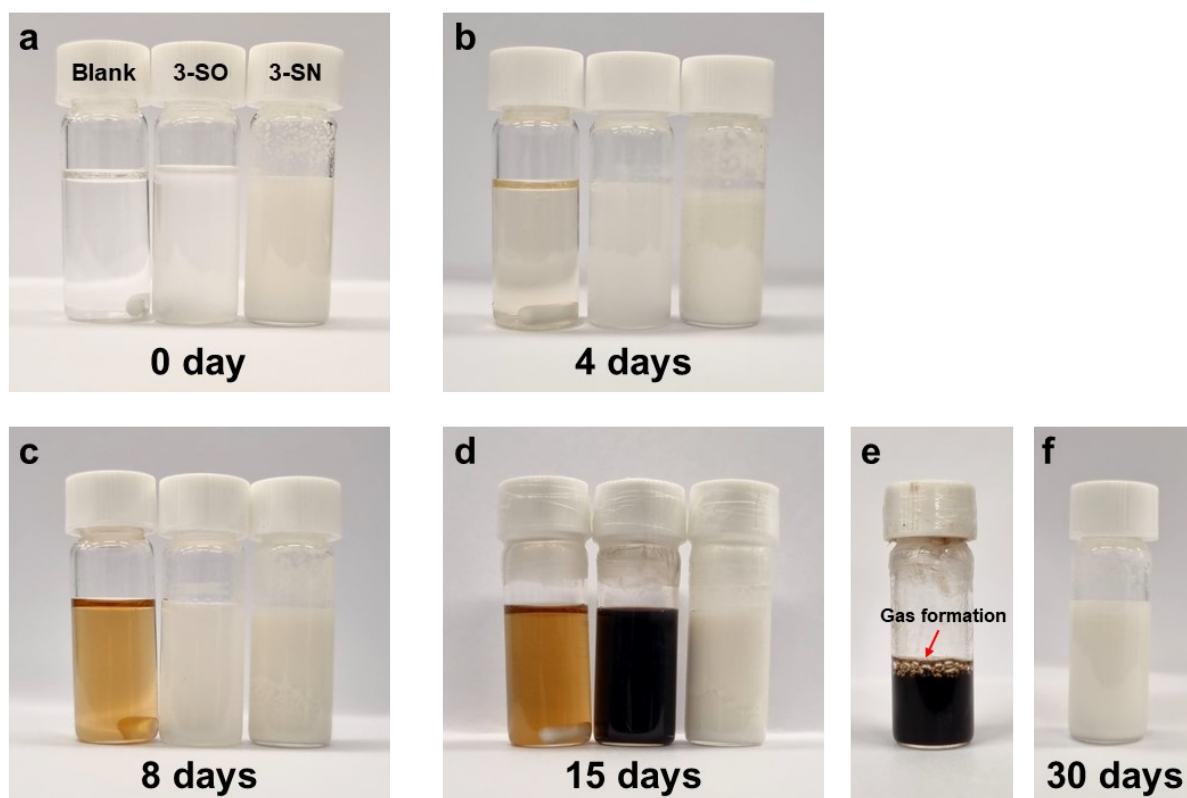


**Fig. S45.** Chemical stability test of the electrolytes. Electrolytes were vigorously stirred (1150 rpm) on the ambient air at 40 °C. **(a)** 0 day (initial state). **(b)** After 4 days. **(c)** after 8 days. **(d)** after 15 days. **(e)** after opening the cap of the 3-SO vial (15 days). After opening the cap, the electrolyte immediately explodes and overflows, and the gas bubbles were observed. **(f)** After 30 days (3-SN).

**Note)** As shown in **Fig. S45**, the chemical stability of 3-SN surpassed that of both the Blank and 3-SO. The discoloration observed in the Blank, which results from the hydrolysis of  $\text{LiPF}_6$  and the dehydrofluorination of FEC, began only after 4 days of vigorous stirring and exposure to elevated temperatures in ambient air. In contrast, 3-SO did not show any color change until 8 days, but suddenly turned black after 15 days. In contrast, 3-SO did not show any color change until day 8, but suddenly turned black after 15 days. Furthermore, it exploded and overflowed with gas bubbles immediately upon opening the vial, presumably due to the formation of gaseous byproducts. As mentioned in the main text, silica can scavenge HF but forms excess  $\text{SiF}_4$  gas as shown below<sup>26</sup>:



$\text{SiF}_4$  gas can cause further side reactions with battery components, such as the SEI layer, leading to battery swelling. Moreover, the  $\text{H}_2\text{O}$  byproduct accelerates the hydrolysis of  $\text{LiPF}_6$ .

In contrast,  $\text{Si}_3\text{N}_4$  did not show any color change even after 15 days. Several published studies demonstrate that the Si-N bond scavenges HF, forming Si-F and N-H bonds, suggesting the application of these electrolyte additives in LIBs as HF scavengers.<sup>27-29</sup> Similarly,  $\text{Si}_3\text{N}_4$  is known to form Si-F and N-H bonds through the HF etching mechanism<sup>30</sup> and can even produce  $(\text{NH}_4)_2\text{SiF}_6$  on its surface<sup>31</sup>, enabling it to scavenge a larger amount of HF compared to  $\text{SiO}_2$ . Our DFT results also reveal that the HF scavenging mechanisms, which involve the formation

of stable Si–F and N–H bonds on the surface of nano-Si<sub>3</sub>N<sub>4</sub>, are thermodynamically favorable (**Fig. S34**). The formation of stable Si-F and N-H bonds renders the HF scavenging mechanism irreversible. Furthermore, the final products of the HF scavenging mechanism are (NH<sub>4</sub>)<sub>2</sub>SiF<sub>6</sub> (s) and SiF<sub>4</sub> (g), preventing the reverse reaction. Additionally, unlike SiO<sub>2</sub>, Si<sub>3</sub>N<sub>4</sub> does not produce H<sub>2</sub>O through HF scavenging mechanisms, which prevents the accelerated degradation of the electrolyte (hydrolysis of LiPF<sub>6</sub>).



These differences in chemical reactions are the reason why 3-SN exhibits much better cyclability at high voltages and temperatures than 3-SO.



**Fig. S46.** Visualization of electrolyte sedimentation. **(a)** Long-term storage of 3-SN. **(b)** After 10 vigorous shakes following 1 month of storage as shown in **(a)**. **(c)**, **(d)** Other suspension electrolytes containing 3 wt% solid particles, including silica, cobalt oxide, titanium oxide and Li<sub>3</sub>N. The silica in **(c)** corresponds to 3-SO. 3-SN demonstrates significantly slower sedimentation compared to other electrolytes, and effectively prevents electrolyte discoloration after 1 month storage.

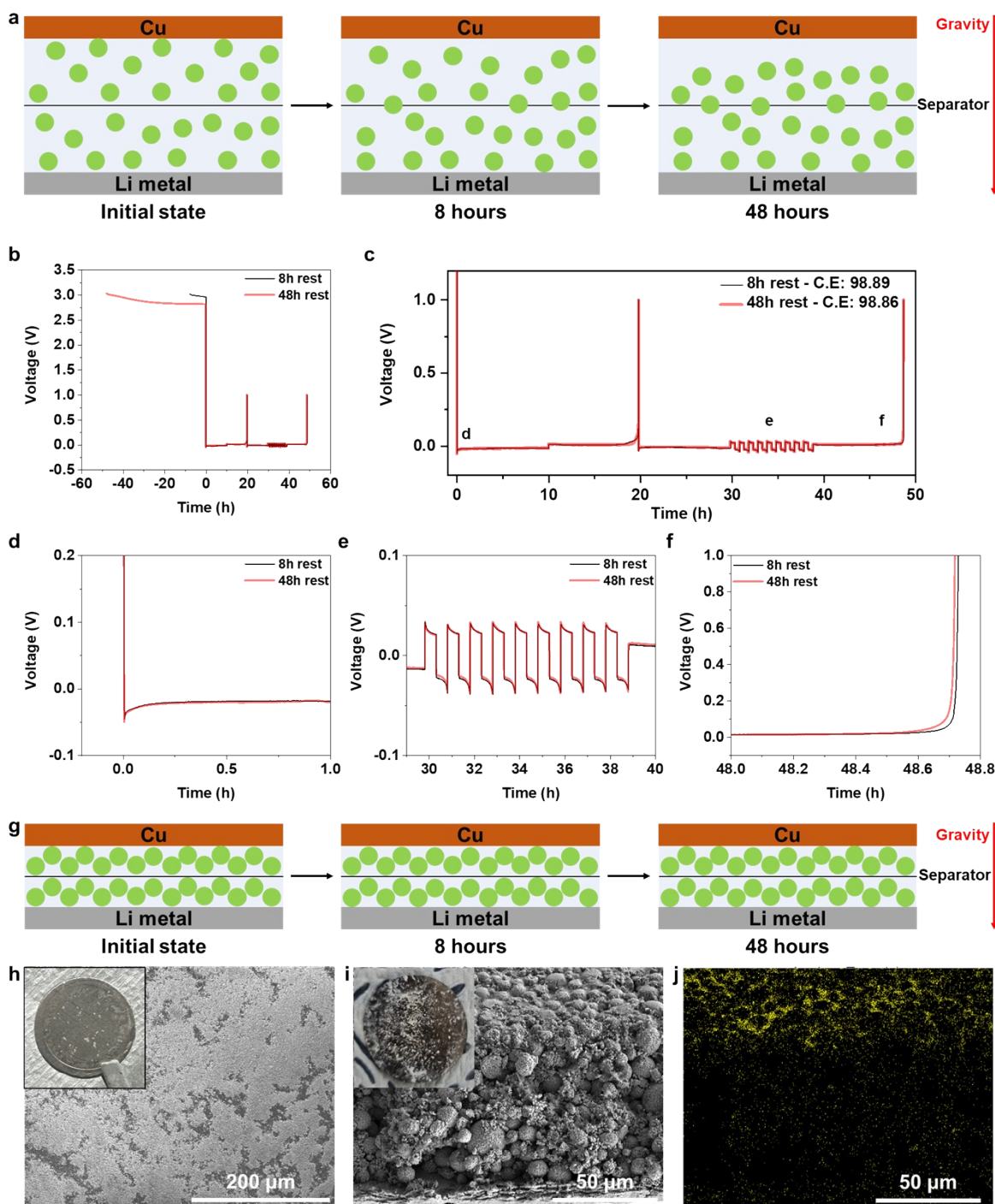


**Fig. S47.** (a) Experimental setup for investigating the effect of sedimentation on electrochemical performance. (b), (c) Voltage profiles from Modified Aurbach's Coulombic efficiency tests with two different rest times. (d) Enlargement of (c) for displaying nucleation overpotential. Modified Aurbach's Coulombic efficiency tests were conducted at  $0.5 \text{ mA cm}^{-2}$ . (e) Enlargement of (c) for displaying symmetric cycling region, conducted at  $2 \text{ mA cm}^{-2}$  and  $1 \text{ mA h cm}^{-2}$ . (f) Enlargement of (c) for displaying Coulombic efficiency. (g) Realistic schematic illustration of sedimentation effects in a coin-cell under high pressure. (h) Digital photograph and SEM image of Li metal after cell disassembly without cycling. (i) Digital photograph and SEM image of NCM811 retrieved from Li||NCM811 after 50 cycles under 4.5-3.0V and 0.5C, 1D. Despite thorough washing with DEC, nano-Si<sub>3</sub>N<sub>4</sub> remained adhered to both the Li metal and cathode surface. (j) Si Energy Dispersive X-ray Spectroscopy (EDX) mapping image corresponding to Fig. S47i.

**Note)** For 3-SN, sedimentation occurred gradually. Even after 24 hours, the appearance of 3-SN remained unchanged from its initial state. After 48 hours, a transparent supernatant layer began to form, and this layer continued to thicken over the course of 1 month (**Fig. S46a**). Additionally, after 1 month, discoloration was observed in all samples except for 3-SN, indicating that nano-Si<sub>3</sub>N<sub>4</sub> in 3-SN effectively scavenged HF, thereby enhancing the chemical stability of the electrolyte. Upon shaking the vial 10 times (**Fig. S46b**), the nano-Si<sub>3</sub>N<sub>4</sub>-based suspension electrolytes readily redispersed, demonstrating their reusability even after complete sedimentation.

In contrast, the oxide-based suspension electrolytes and the previously reported Li<sub>3</sub>N-based suspension electrolyte exhibited rapid sedimentation, with most particles settling within 1 hour (**Fig. S46c, d**). Such rapid sedimentation can result in an inhomogeneous distribution of particles within the battery, which increases the non-uniformity of electrochemical performance.

To further evaluate the impact of sedimentation on electrochemical performance, we designed Li||Cu half-cell tests. If sedimentation significantly influenced electrochemical performance, we would expect to observe variations based on the rest time before operation (**Fig. S47a**). However, the rest time had a negligible effect on electrochemical performances, including Coulombic efficiency and overpotentials (**Fig. S47b-f**). This finding suggests that the gradual sedimentation of nano-Si<sub>3</sub>N<sub>4</sub> does not critically affect electrochemical performance.

We hypothesize that the high pressure within the cell helps maintain a consistent concentration of nano-Si<sub>3</sub>N<sub>4</sub> (*i.e.*, contact between electrodes and nano-Si<sub>3</sub>N<sub>4</sub>) between the electrodes (**Fig. S47g**). Due to the high pressure applied to the electrodes, nano-Si<sub>3</sub>N<sub>4</sub> remained adhered to both the Li metal and cathode surfaces, even after thorough washing (**Fig. S47h-j**).

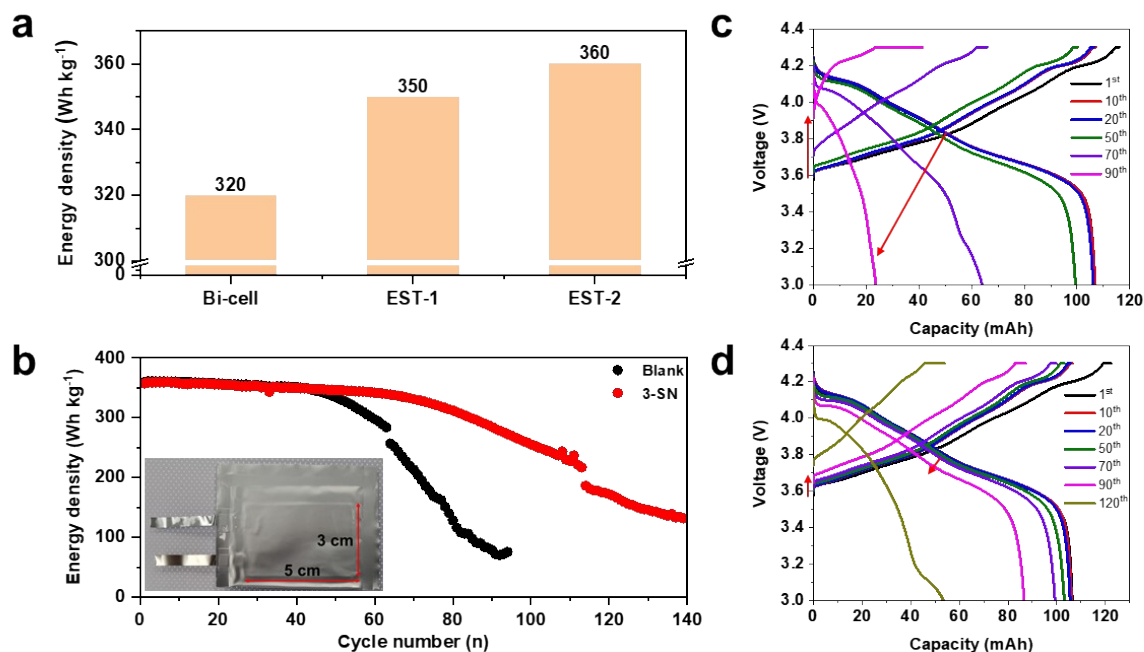


**Fig. S48.** (a) Estimated energy density of practical-level pouch cell. The bi-cell consists of one sheet of a double-side coated NCM811 cathode, two sheets of Cu current collector and Li anode, two sheets of separator, and an electrolyte. For EST-1, a 30-stacked of bi-cell is assumed. For EST-2, the thickness of the Cu current collector is assumed to be 5  $\mu\text{m}$ , as it is commercially available. This estimation aims to reduce the weight ratio of the Cu current collector in the total cell weight, reflecting practical-level cell design. (b) Calculated energy density using EST-2 for the Blank and 3-SN. The detail parameters are provided in **Table S9**. (c), (d) Voltage profile of the Blank in (b). (c) Blank, (d) 3-SN.

**Note)** In the case of the Blank, the IR drop and ohmic polarization increased drastically after 50 cycles. The concurrent increase in both IR drop and ohmic polarization suggests the accumulation of a resistive film on both the anode and cathode during cycling, likely due to the formation of thick and inhomogeneous SEI and CEI layers.

In contrast, 3-SN demonstrates high resistance to chemical corrosion (**Fig. S24**) and promotes spherical, dense Li deposition, resulting in a reduced surface area compared to the Blank (**Fig. 4h–k**). Consequently, the increase in interfacial resistance with 3-SN is significantly lower than that with the Blank (**Fig. S9**), leading to much better cyclability. Nevertheless, EC-based carbonate electrolytes suffer from high reactivity with Li metal due to their low LUMO (Lowest Unoccupied Molecular Orbital) level, which results in a gradual capacity decline after 80 cycles, even with 3-SN.

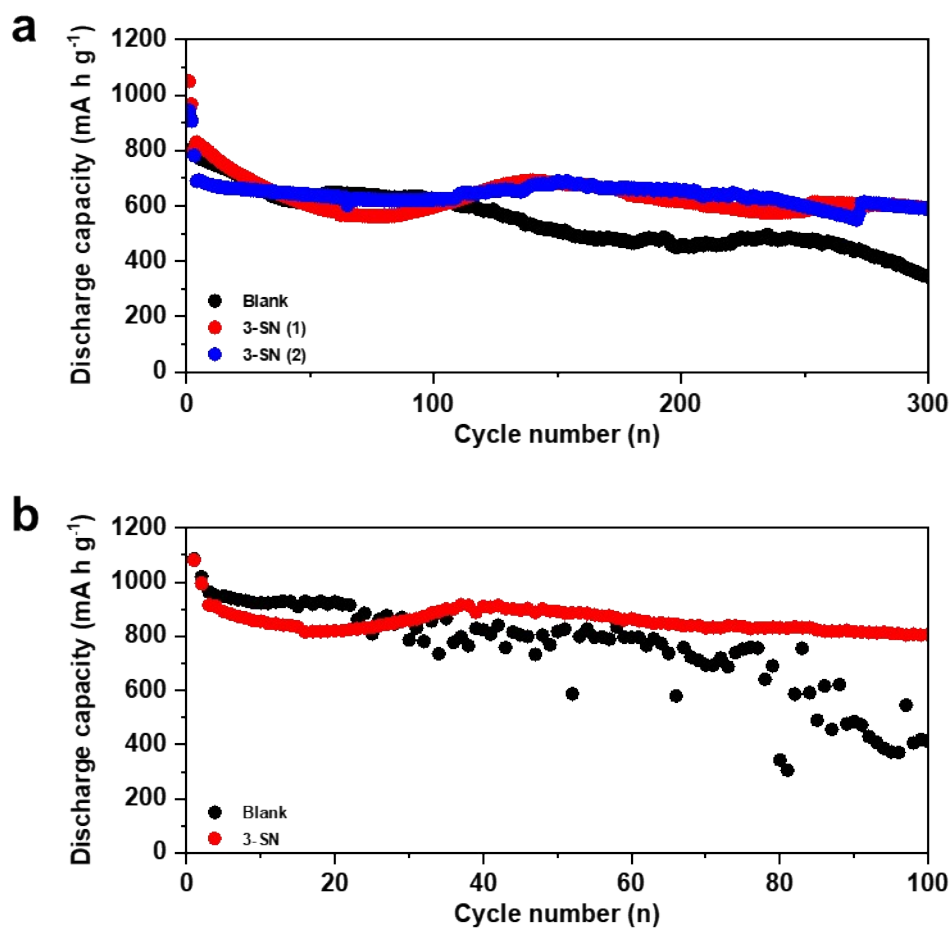


**Fig. S49.** Electrochemical test results of Li||S full-cell. Blank electrolyte: 1M LiTFSI DOL/DME + 2 wt% LiNO<sub>3</sub>. **(a)** Sulfur loading: 1.5mg<sub>s</sub> cm<sup>-2</sup>, E/S = 10 μL mg<sup>-1</sup>, 0.3C/D cycling. **(b)** Sulfur loading: 4 mg<sub>s</sub> cm<sup>-2</sup>, E/S = 6, 0.1C/D cycling.

### 3. Supplementary Tables

**Table S1.** A summary of electrochemical performances of the published work on suspension, and colloid electrolytes for lithium metal batteries

Electrolyte	Electrolyte Amount (E/C ratio)	Cell configurations	Cycling condition & cyclability
(1M LiPF <sub>6</sub> EC/DEC + 10 vol % FEC) + 7 wt% Li <sub>2</sub> O (80-100 nm) <sup>21</sup>	5 ml Ah <sup>-1</sup>	500 μm Li 4 mA h cm <sup>-2</sup> NCM811, N/P = 25	0.5C/1D, 3.0-4.3V, 150 cycles (coin-cell)
(1M LiPF <sub>6</sub> EC/DEC + 10 vol % FEC) + 7 wt% Li <sub>3</sub> N (80-100 nm) <sup>32</sup>	5 ml Ah <sup>-1</sup>	750 μm Li 4 mA h cm <sup>-2</sup> NCM811, N/P = 62.5	0.5C/1D, 3.0-4.3V, 150 cycles (coin-cell)
(1M LiPF <sub>6</sub> EC/DEC) + 3 wt% CaCO <sub>3</sub> (40-80 nm) + 0.7 wt% X-100 <sup>33</sup>	4.4 g Ah <sup>-1</sup>	50 μm Li 3.4 mA h cm <sup>-2</sup> LFP, N/P = 2.9	0.5C/0.5D, 2-3.9V, 60 cycles (coin-cell)
			Light bulb on (pouch-cell)
(1M LiPF <sub>6</sub> EC/EMC + 2 wt% VC + SiO <sub>2</sub> (7 nm, 15 mg mL <sup>-1</sup> ) <sup>26</sup>	75 μL (flooded)	40 μm Li 4.2 mA h cm <sup>-2</sup> NCM 811, N/P = 1.9	0.2C/0.5D, 3.0-4.3V, 100 cycles, 70% (coin-cell)
0.6M LiPF <sub>6</sub> , 0.6M LiDFOB FEC/DEC (1:2) + citric acid (CA)-modified SiO <sub>2</sub> (7 nm, 15 mg mL <sup>-1</sup> ) <sup>34</sup>	6 g Ah <sup>-1</sup>	50 μm Li 4.8 mA h cm <sup>-2</sup> NCM 811, N/P = 2.1	0.2C/0.5D, 3.0-4.3V, 110 cycle (70%), coin-cell
	6 g Ah <sup>-1</sup>	50 μm Li 4.8 mA h cm <sup>-2</sup> NCM 811, N/P = 2.1	0.5C/1D, 3.0-4.3V, 60 cycle (60%) pouch-cell
1M LiPF <sub>6</sub> EC/DEC + MLE-100 (Al) (0.25g mL <sup>-1</sup> ) <sup>35</sup>	100 μL (flooded)	50 μm Li 3.3 mA h cm <sup>-2</sup> NCA, N/P = 3	0.33C/0.33D, 3.0-4.3V, 200 cycle (83%), coin-cell
(1M LiPF <sub>6</sub> EC/DEC + 5 vol% FEC) + 0.4 wt% Al(OEt) <sub>3</sub> nanowire <sup>36</sup>	3.4 g Ah <sup>-1</sup>	40 μm Li 4 mA h cm <sup>-2</sup> NCM111, N/P = 2.13	0.1C/0.3D, 3.0-4.5V, 130 cycle (80.3%), coin-cell
<b>This work</b>	<b>4 ml Ah<sup>-1</sup></b>	<b>50 μm Li ~4 mA h cm<sup>-2</sup> NCM811, N/P = 2.5</b>	<b>0.2C/0.5D, 3.0-4.3V, 150 cycle (85%), coin-cell</b>
	<b>4 ml Ah<sup>-1</sup></b>	<b>50 μm Li ~4 mA h cm<sup>-2</sup> NCM811, N/P = 2.5</b>	<b>0.2C/0.5D, 3.0-4.5V, 100 cycle (80%), coin-cell</b>
	<b>2.5 g Ah<sup>-1</sup></b>	<b>40 μm Li ~4 mA h cm<sup>-2</sup> NCM811, N/P = 2</b>	<b>0.2C/0.5D, 3.0-4.3V, 80 cycle (86%), 360 Wh kg<sup>-1</sup>-level pouch-cell</b>

**Table S2.** Nucleation overpotential and Coulombic efficiency of various x-SNs, based on **Fig. S3**.

	<b>Nucleation overpotential (mV)</b>	<b>C.E. (%)</b>
<b>Blank</b>	<b>98.9</b>	<b>95.79</b>
<b>0.1-SN</b>	<b>55.8</b>	<b>98.05</b>
<b>0.5-SN</b>	<b>51.1</b>	<b>98.29</b>
<b>1-SN</b>	<b>50.5</b>	<b>98.53</b>
<b>3-SN</b>	<b>47.1</b>	<b>98.62</b>
<b>5-SN</b>	<b>43.1</b>	<b>98.59</b>

**Table S3.** EIS results of the Blank from Fig. S9.

<b>Blank</b>	<b>0 cyc</b>	<b>1 cyc</b>	<b>5 cyc</b>	<b>9 cyc</b>	<b>13 cyc</b>	<b>17 cyc</b>	<b>21 cyc</b>	<b>25 cyc</b>	<b>29 cyc</b>	<b>33 cyc</b>	<b>37 cyc</b>	<b>41 cyc</b>
<b>R<sub>sol</sub> (Ohm)</b>	<b>1.081</b>	<b>1.203</b>	<b>1.501</b>	<b>1.597</b>	<b>1.69</b>	<b>1.861</b>	<b>2.095</b>	<b>2.324</b>	<b>2.575</b>	<b>3.029</b>	<b>4.182</b>	<b>5.345</b>
<b>R<sub>SEI</sub></b>	<b>32.52</b>	<b>9.241</b>	<b>7.204</b>	<b>6.252</b>	<b>5.761</b>	<b>5.352</b>	<b>4.87</b>	<b>4.951</b>	<b>5.166</b>	<b>9.698</b>	<b>16.30</b>	<b>21.55</b>
<b>R<sub>ct</sub></b>	<b>10.65</b>	<b>18.96</b>	<b>16.43</b>	<b>15.87</b>	<b>16.04</b>	<b>17.68</b>	<b>19.46</b>	<b>22.41</b>	<b>28.26</b>	<b>41.16</b>	<b>44.12</b>	<b>41.94</b>
<b>R<sub>tot</sub> (R<sub>SEI</sub> + R<sub>ct</sub>)</b>	<b>43.17</b>	<b>28.20</b>	<b>23.63</b>	<b>22.12</b>	<b>21.80</b>	<b>23.03</b>	<b>24.33</b>	<b>27.36</b>	<b>33.43</b>	<b>50.86</b>	<b>60.42</b>	<b>63.49</b>

**Table S4.** EIS results of 3-SN from Fig. S9.

<b>3-SN</b>	<b>0 cyc</b>	<b>1 cyc</b>	<b>5 cyc</b>	<b>9 cyc</b>	<b>13 cyc</b>	<b>17 cyc</b>	<b>21 cyc</b>	<b>25 cyc</b>	<b>29 cyc</b>	<b>33 cyc</b>	<b>37 cyc</b>	<b>41 cyc</b>
<b>R<sub>sol</sub> (Ohm)</b>	<b>1.119</b>	<b>1.192</b>	<b>1.272</b>	<b>1.329</b>	<b>1.377</b>	<b>1.415</b>	<b>1.446</b>	<b>1.509</b>	<b>1.579</b>	<b>1.689</b>	<b>1.843</b>	<b>2.014</b>
<b>R<sub>SEI</sub></b>	<b>10.65</b>	<b>4.525</b>	<b>4.431</b>	<b>4.044</b>	<b>3.547</b>	<b>2.992</b>	<b>2.462</b>	<b>2.382</b>	<b>2.242</b>	<b>2.449</b>	<b>2.879</b>	<b>3.447</b>
<b>R<sub>ct</sub></b>	<b>22.04</b>	<b>14.11</b>	<b>13.02</b>	<b>12.6</b>	<b>11.87</b>	<b>11.82</b>	<b>11.73</b>	<b>12.32</b>	<b>12.61</b>	<b>13.57</b>	<b>14.95</b>	<b>16.39</b>
<b>R<sub>tot</sub> (R<sub>SEI</sub> + R<sub>ct</sub>)</b>	<b>32.69</b>	<b>18.64</b>	<b>17.45</b>	<b>16.64</b>	<b>15.42</b>	<b>14.81</b>	<b>14.19</b>	<b>14.70</b>	<b>14.85</b>	<b>16.02</b>	<b>17.83</b>	<b>19.84</b>

**Table S5.**  $R_{\text{int}}(0)$ , a, b,  $R^2$  value of the Blank and 3-SN from **Fig. S24**.

$R_{\text{int}}(t) = R_{\text{int}}(0) + at^b$	$R_{\text{int}}(0)$	a	b	$R^2$
Blank	38.19205	18.61053	0.34186	0.99651
3-SN	28.40560	18.55808	0.30873	0.99214

**Table S6.** Nucleation overpotential and Coulombic efficiency of various nitride additives in the Blank, based on the **Fig. S10**.

	<b>Nucleation overpotential (mV)</b>	<b>C.E. (%)</b>
<b>Blank</b>	<b>98.9</b>	<b>95.79</b>
<b>BN</b>	<b>78.6</b>	<b>94.87</b>
<b>TiN</b>	<b>62.5</b>	<b>96.29</b>
<b>VN</b>	<b>65.9</b>	<b>Short-circuit</b>
<b>Si<sub>3</sub>N<sub>4</sub></b>	<b>47.1</b>	<b>98.62</b>

**Table S7.** Number of molecule participating in the solvation within 3 Å distance around Li<sup>+</sup> ions, which is related to **Fig. 3b**. The number of Li<sup>+</sup> ions is 16, which is selected by the distance criterion of 5 Å from the surface of Si<sub>3</sub>N<sub>4</sub>, to investigate the solvation environment nearby the nano-Si<sub>3</sub>N<sub>4</sub>. For the Blank condition, the sixteen Li<sup>+</sup> ions were randomly selected to compare the 3-SN condition system.

Condition	EC	DEC	FEC	PF <sub>6</sub>	(Si <sub>3</sub> N <sub>4</sub> ) <sub>10</sub>
Blank	24	15	2	1	-
3-SN	14	8	1	1	12

**Table S8.** A list of possible chemical species and their corresponding d-spacing values observed in Cryo-TEM images (**Fig. 4**, **Fig. 5**, and **Fig. S25**).

	(hkl)	d spacing (Å)
Li <sub>2</sub> O (Fm-3m, cubic)	(111)	2.687
	(200)	2.327
	(220)	1.645
LiF (Fm-3m, cubic)	(111)	2.358
	(200)	2.042
	(220)	1.444
Li <sub>2</sub> CO <sub>3</sub> (C12/c1, monoclinic)	(110)	4.156
	(200)	3.791
	(111)	3.024
Li <sub>2</sub> CO <sub>3</sub> (P6 <sub>3</sub> /mcm, hexagonal)	(10-10)	4.03
	(0002)	2.691
Li <sub>3</sub> N (P6/mmm, hexagonal)	(0001)	3.855
	(10-10)	3.126
Li <sub>3</sub> N (P6 <sub>3</sub> /mmc, hexagonal)	(0002)	3.13
	(10-10)	3.052
	(10-11)	2.743
Li metal (Im-3m, cubic)	(111)	2.432
	(200)	1.72
	(220)	1.404
Li <sub>13</sub> Si <sub>4</sub> (Pbam, orthorhombic)	(013)	4.227
	(020)	3.952
Li <sub>15</sub> Si <sub>4</sub> (I4-3d, Cubic)	(211)	<b>4.309</b>
	(220)	3.732
	(310)	3.338

**Table S9.** Detailed parameters of the pouch cells.

	<b>Bi-cell (Experimental)</b>	<b>EST-1</b>	<b>EST-2</b>
<b>NCM811</b>	18.78 mg cm <sup>-2</sup>	18.78 mg cm <sup>-2</sup>	18.78 mg cm <sup>-2</sup>
<b>Al current collector (13 μm)</b>	3.51 mg cm <sup>-2</sup>	3.51 mg cm <sup>-2</sup>	3.51 mg cm <sup>-2</sup>
<b>Li metal (40 μm)</b>	2.14 mg cm <sup>-2</sup>	2.14 mg cm <sup>-2</sup>	2.14 mg cm <sup>-2</sup>
<b>Cu current collector</b>	8 μm Cu: 7.12 mg cm <sup>-2</sup>	8 μm Cu: 7.12 mg cm <sup>-2</sup>	5 μm Cu: 4.45 mg cm <sup>-2</sup>
<b>Separator (Celgard 2400)</b>	1.14 mg cm <sup>-2</sup>	1.14 mg cm <sup>-2</sup>	1.14 mg cm <sup>-2</sup>
<b>Electrolyte</b>	2.5 g Ah <sup>-1</sup>	2.5 g Ah <sup>-1</sup>	2.5 g Ah <sup>-1</sup>
<b>Tap, Pouch case</b>	Estimated to 3 wt% of total cell weight	Estimated to 3 wt% of total cell weight	Estimated to 3 wt% of total cell weight
<b>Total cell weight</b>	1.27 g	35.18 g	33.90 g
<b>Discharge Capacity</b>	Blank: 106.8 mAh	Blank: 3.204 Ah	Blank: 3.204 Ah
	3-SN: 107.4 mAh	3-SN: 3.222 Ah	3-SN: 3.222 Ah
<b>Average discharge voltage</b>	Blank: 3.80 V	Blank: 3.80 V	Blank: 3.80 V
	3-SN: 3.80 V	3-SN: 3.80 V	3-SN: 3.80 V
<b>Gravimetric energy density</b>	Blank: 320 Wh kg <sup>-1</sup>	Blank: 346 Wh kg <sup>-1</sup>	Blank: 359 Wh kg <sup>-1</sup>
	<b>3-SN : 321 Wh kg<sup>-1</sup></b>	<b>3-SN : 348 Wh kg<sup>-1</sup></b>	<b>3-SN : 361 Wh kg<sup>-1</sup></b>

#### 4. Supplementary Note

##### Note S1. The detailed mechanisms of H-transfer reactions of ethylene carbonate (EC).

The mechanism of the H-transfer reaction remains unclear and is still veiled in ambiguity. According to the Yang Shao Horn's group, electrophilic attack and H-transfer reactions are energetically favorable oxidative decomposition pathways of ethylene carbonate (EC) on the  $\text{LiMO}_2$  ( $M = \text{Mn, Fe, Co, Ni}$ ) surface<sup>37</sup>. Moreover, the H-transfer reaction became increasingly favorable as  $\text{LiMO}_2$  underwent further delithiation, and  $\text{LiNiO}_2$  was identified as the most favorable cathode material. The detailed mechanisms of the H-transfer reaction are as follows<sup>37</sup>:



$* \text{C}_3\text{O}_3\text{H}_3$  and  $* \text{H}$  represent the EC decomposition products adsorbed on the lattice oxygens at the surface of the cathodes.

In this case, the C-H bond dissociation energy of the EC is a critical factor for the degree of the H-transfer reaction. Therefore, nano- $\text{Si}_3\text{N}_4$  played a significant role in mitigating the H-transfer reaction, owing to its interaction with free-EC.

According to the recent report by Xiangming He's group, the H-transfer reaction mechanism initiates from the oxygen atom in the C=O bond of EC adsorbed onto the surface of the cathodes, followed by the transfer of a hydrogen atom from the EC to the oxygen site of NCM811<sup>38</sup>. They also argued that the Ni site in NCM811 had a significant catalytic effect on the H-transfer reaction of EC because it showed the lowest reaction energy for the H-transfer step.

In this case, nano- $\text{Si}_3\text{N}_4$  can mitigate the H-transfer reaction because the C=O in EC has already interacted with the nano- $\text{Si}_3\text{N}_4$ . For the H-transfer reaction of the bound-EC to take place, additional reaction energy was required to release the interaction between the pre-existing EC and nano- $\text{Si}_3\text{N}_4$ .

Both proposed mechanisms result in the formation of an -OH bond on the lattice oxygen of the NCM811 surface. This leads to an extension of the Ni-O bond length, which weakens the Ni-O bond. Weakened Ni-O bonds accelerate the  $\text{Ni}^{2+}$  dissolution from NCM811.

Simultaneously, the -OH group detaches from the surface and reacts with the hydrogen species to produce  $\text{H}_2\text{O}$ . This leads to the hydrolysis of  $\text{LiPF}_6$ , forming HF, which subsequently attacks both the cathode-electrolyte interphase (CEI) layer and the cathode (**Fig. 5e-h**), leading to rapid cell failure.

Furthermore, the fragments of EC adsorbed onto the NCM811 surface underwent oxidative decomposition, producing CO and  $\text{CO}_2$ . These gas products exacerbate cell expansion and safety concerns.

In summary, the H-transfer reaction of EC on the NCM811 surface leads to multiple detrimental effects, including  $\text{Ni}^{2+}$  dissolution, HF production, and the generation of gaseous CO and  $\text{CO}_2$ , all of which contribute to the degradation of the electrochemical performance of lithium metal batteries.

## 5. Supplementary References

1. D. T. Boyle, W. Huang, H. Wang, Y. Li, H. Chen, Z. Yu, W. Zhang, Z. Bao and Y. Cui, *Nat. Energy*, 2021, **6**, 487-494.
2. S. C. Kim, X. Kong, R. A. Vila, W. Huang, Y. Chen, D. T. Boyle, Z. Yu, H. Wang, Z. Bao, J. Qin and Y. Cui, *J. Am. Chem. Soc.*, 2021, **143**, 10301-10308.
3. A. Jain, S. P. Ong, G. Hautier, W. Chen, W. D. Richards, S. Dacek, S. Cholia, D. Gunter, D. Skinner, G. Ceder and K. A. Persson, *APL Mater.*, 2013, **1**, 011002.
4. U. C. Singh and P. A. Kollman, *J. Comput. Chem.*, 1984, **5**, 129-145.
5. C. Park, M. Kanduč, R. Chudoba, A. Ronneburg, S. Risse, M. Ballauff and J. Dzubiella, *J. Power Sources*, 2018, **373**, 70-78.
6. I. Leontyev and A. Stuchebrukhov, *Phys. Chem. Chem. Phys.*, 2011, **13**, 2613-2626.
7. R. L. C. Akkermans, N. A. Spenley and S. H. Robertson, *Mol. Simul.*, 2021, **47**, 540-551.
8. H. J. C. Berendsen, J. P. M. Postma, W. F. van Gunsteren, A. DiNola and J. R. Haak, *J. Chem. Phys.*, 1984, **81**, 3684-3690.
9. B. Delley, *J. Chem. Phys.*, 1990, **92**, 508-517.
10. B. Delley, *J. Chem. Phys.*, 2000, **113**, 7756-7764.
11. A. D. Becke, *J. Chem. Phys.*, 1993, **98**, 5648-5652.
12. P. J. Stephens, F. J. Devlin, C. F. Chabalowski and M. J. Frisch, *J. Phys. Chem.*, 1994, **98**, 11623-11627.
13. A. Tkatchenko and M. Scheffler, *Phys. Rev. Lett.*, 2009, **102**, 073005.
14. A. Klamt and G. Schüürmann, *J. Chem. Soc. Perkin Trans. 2*, 1993, 799-805.
15. D. S. Hall, J. Self and J. R. Dahn, *J. Phys. Chem. C*, 2015, **119**, 22322-22330.
16. H. Looyenga, *Physica*, 1965, **31**, 401-406.
17. S. J. Clark, M. D. Segall, C. J. Pickard, P. J. Hasnip, M. I. J. Probert, K. Refson and M. C. Payne, *Z. Kristallogr. Cryst. Mater.*, 2005, **220**, 567-570.
18. J. P. Perdew, K. Burke and M. Ernzerhof, *Phys. Rev. Lett.*, 1996, **77**, 3865.
19. H. J. Monkhorst and J. D. Pack, *Phys. Rev. B*, 1976, **13**, 5188.
20. B. Han, Z. Zhang, Y. Zou, K. Xu, G. Xu, H. Wang, H. Meng, Y. Deng, J. Li and M. Gu, *Adv. Mater.*, 2021, **33**, 2100404.
21. M. S. Kim, Z. Zhang, P. E. Rudnicki, Z. Yu, J. Wang, H. Wang, S. T. Oyakhire, Y. Chen, S. C. Kim, W. Zhang, D. T. Boyle, X. Kong, R. Xu, Z. Huang, W. Huang, S. F. Bent, L. W. Wang, J. Qin, Z. Bao and Y. Cui, *Nat. Mater.*, 2022, **21**, 445-454.
22. Q. Cheng, A. Li, N. Li, S. Li, A. Zangiabadi, T.-D. Li, W. Huang, A. C. Li, T. Jin, Q. Song, W. Xu, N. Ni, H. Zhai, M. Dontigny, K. Zaghbi, X. Chuan, D. Su, K. Yan and Y. Yang, *Joule*, 2019, **3**, 1510-1522.
23. W. G. Lim, C. Jo, A. Cho, J. Hwang, S. Kim, J. W. Han and J. Lee, *Adv. Mater.*, 2019, **31**, 1806547.
24. S. Park, S. Kim, J. A. Lee, M. Ue and N. S. Choi, *Chem. Sci.*, 2023, **14**, 9996-10024.
25. K. Kim, I. Park, S.-Y. Ha, Y. Kim, M.-H. Woo, M.-H. Jeong, W. C. Shin, M. Ue, S. Y. Hong and N.-S. Choi, *Electrochim. Acta*, 2017, **225**, 358-368.
26. J. Lee, H. S. Lim, X. Cao, X. Ren, W. J. Kwak, I. A. Rodriguez-Perez, J. G. Zhang, H. Lee and H. T. Kim, *ACS Appl. Mater. Interfaces*, 2020, **12**, 37188-37196.
27. K. Kim, D. Hwang, S. Kim, S. O. Park, H. Cha, Y. S. Lee, J. Cho, S. K. Kwak and N. S. Choi, *Adv. Energy Mater.*, 2020, **10**, 2000012.
28. J.-G. Han, M.-Y. Jeong, K. Kim, C. Park, C. H. Sung, D. W. Bak, K. H. Kim, K.-M. Jeong and N.-S. Choi, *J. Power Sources*, 2020, **446**, 227366.
29. J. G. Han, K. Kim, Y. Lee and N. S. Choi, *Adv. Mater.*, 2019, **31**, 1804822.
30. D. M. Knotter and T. D. Denteneer, *J. Electrochem. Soc.*, 2001, **148**, F43.
31. H.-J. Kwon and J.-G. Park, *J. Korean Phys. Soc.*, 2022, **81**, 903-909.
32. M. S. Kim, Z. Zhang, J. Wang, S. T. Oyakhire, S. C. Kim, Z. Yu, Y. Chen, D. T. Boyle, Y. Ye, Z. Huang, W. Zhang, R. Xu, P. Sayavong, S. F. Bent, J. Qin, Z. Bao and Y. Cui, *ACS Nano*, 2023, **17**, 3168-3180.
33. Q. Peng, Z. Liu, L. Jiang and Q. Wang, *Adv. Energy Mater.*, 2022, **12**, 2104021.
34. M. Lim, H. An, J. Seo, M. Lee, H. Lee, H. Kwon, H. T. Kim, D. Esken, R. Takata, H. A. Song and H. Lee, *Small*, 2023, **19**, 2302722.
35. L. Shen, H. B. Wu, F. Liu, J. Shen, R. Mo, G. Chen, G. Tan, J. Chen, X. Kong, X. Lu, Y. Peng, J. Zhu, G. Wang and Y. Lu, *Adv. Funct. Mater.*, 2020, **30**, 2003055.
36. Y. Zhang, Y. Wu, H. Li, J. Chen, D. Lei and C. Wang, *Nat. Commun.*, 2022, **13**, 1297.
37. L. Giordano, P. Karayaylali, Y. Yu, Y. Katayama, F. Maglia, S. Lux and Y. Shao-Horn, *J. Phys. Chem. Lett.*, 2017, **8**, 3881-3887.
38. X. Wang, D. Ren, H. Liang, Y. Song, H. Huo, A. Wang, Y. Gao, J. Liu, Y. Gao, L. Wang and X. He, *Energy Environ. Sci.*, 2023, **16**, 1200-1209.